CARRIER FREQUENCY OFFSET RECOVERY FOR ZERO-IF OFDM RECEIVERS

A Thesis Submitted
to the College of Graduate Studies and Research
in Partial Fulfillment of the Requirements
for the Degree of Master of Science
in the Department of Electrical Engineering
University of Saskatchewan
Saskatoon

by

Michael Mitzel

PERMISSION TO USE

In presenting this thesis in partial fulfillment of the requirements for a Postgraduate degree from the University of Saskatchewan, it is agreed that the Libraries of this University may make it freely available for inspection. Permission for copying of this thesis in any manner, in whole or in part, for scholarly purposes may be granted by the professors who supervised this thesis work or, in their absence, by the Head of the Department of Electrical Engineering or the Dean of the College of Graduate Studies and Research at the University of Saskatchewan. Any copying, publication, or use of this thesis, or parts thereof, for financial gain without the written permission of the author is strictly prohibited. Proper recognition shall be given to the author and to the University of Saskatchewan in any scholarly use which may be made of any material in this thesis.

Request for permission to copy or to make any other use of material in this thesis in whole or in part should be addressed to:

Head of the Department of Electrical Engineering
57 Campus Drive
University of Saskatchewan
Saskatoon, Saskatchewan, Canada
S7N 5A9

ABSTRACT

As trends in broadband wireless communications applications demand faster development cycles, smaller sizes, lower costs, and ever increasing data rates, engineers continually seek new ways to harness evolving technology. The zero intermediate frequency receiver architecture has now become popular as it has both economic and size advantages over the traditional superheterodyne architecture.

Orthogonal Frequency Division Multiplexing (OFDM) is a popular multi-carrier modulation technique with the ability to provide high data rates over echo ladened channels. It has excellent robustness to impairments caused by multipath, which includes frequency selective fading. Unfortunately, OFDM is very sensitive to the carrier frequency offset (CFO) that is introduced by the downconversion process. The objective of this thesis is to develop and to analyze an algorithm for blind CFO recovery suitable for use with a practical zero-Intermediate Frequency (zero-IF) OFDM telecommunications system.

A blind CFO recovery algorithm based upon characteristics of the received signal's power spectrum is proposed. The algorithm's error performance is mathematically analyzed, and the theoretical results are verified with simulations. Simulation shows that the performance of the proposed algorithm agrees with the mathematical analysis.

A number of other CFO recovery techniques are compared to the proposed algorithm. The proposed algorithm performs well in comparison and does not suffer from many of the disadvantages of existing blind CFO recovery techniques. Most notably, its performance is not significantly degraded by noisy, frequency selective channels.

ACKNOWLEDGMENTS

I would like to express my sincere gratitude and appreciation to my supervisor, Dr. J. Eric Salt for his guidance, his teaching, and his continued patience and encouragement throughout the course of Graduate Studies.

I would also like to extend my thanks to the management and staff of TR*Labs* (Saskatoon) for their technical support, for the excellent facilities that they made available to me during the course of my research work, and for their financial assistance in cooperation with The National Science and Engineering Research Council (NSERC).

Finally, I would like to extend special thanks to my mother and my family, for their continued love and endless encouragement. For without them, none of this would have been possible.

Table of Contents

List of Figures

List of Tables

List of Abbreviations

A/D	Analog to Digital
ASIC	Application Specific Integrated Circuit
CFO	Carrier Frequency Offset
D/A	Digital to Analog
DFT	Discrete Fourier Transform
DSP	Digital Signal Processing
IQ	In-Phase and Quadrature
ICI	Inter-Carrier Interference
IDFT	Inverse Discrete Time Fourier Transform
IEEE	Institute of Electrical and Electronic Engineers
IF	Intermediate Frequency
IFFT	Inverse Fast Fourier Transform
ISI	Inter-Symbol Interference
FDM	Frequency Division Multiplexing
FFT	Fast Fourier Transform
FPGA	Field Programmable Gate Array
LAN	Local Area Network
LO	Local Oscillator
LOS	Line of Sight
LNA	Low Noise Amplifier
MAN	Metropolitan Area Network
MSE	Mean Squared Error
OFDM	Orthogonal Frequency Division Multiplexing

PSD	Power Spectral Density
PSK	Phase Shift Keying
QPSK	Quadrature Phase Shift Keying
QAM	Quadrature Amplitude Modulation
RF	Radio Frequency
RFIC	Radio Frequency Integrated Circuit
SAW	Surface Acoustic Wave (Filter)
SNR	Signal to Noise Ratio
SUI	Standford University Interim (Channel Model)

1. INTRODUCTION

Technological advances over the past two decades have led to the rapid evolution of the telecommunications industry. No longer limited to narrow-band voice signals, modern communications integrate voice, images, data, and video on a level that was once considered to be impossible. As applications demand faster development cycles, smaller sizes, and ever increasing data rates, engineers continually seek new ways to harness evolving technology.

1.1 Radio Frequency Receiver Design

Historically, radio frequency (RF) design has been a very complicated and time-consuming process. However, the design of modern radio frequency integrated circuits (RFIC) has become much more easily automated with software tools. This, in turn, has resulted in a shift towards large scale integration becoming an area of increased research activity and commercial interest. While there are a number of obstacles to complete system integration on a single chip, one of particular interest in this work comes from the traditional design limitations of various receiver architectures [1].

The superheterodyne receiver architecture is a well-established topology [2] that down-converts the received signal to one or more intermediate frequencies (IF). These downconverted signals then require extremely selective surface acoustic wave (SAW) filtering to provide adjacent channel filtering and symbol shaping. Unfortunately, this results in a very large surface area requirement which makes high levels of integration impractical for most superheterodyne receivers.

The zero intermediate frequency (zero-IF) architecture provides an attractive alternative to traditional superheterodyne receiver topologies. The concept for the zero-IF receiver, also known as a direct conversion or homodyne receiver, is not a new one. Circuits similar to the direct conversion receivers used today were patented as early as the 1920s, and many variations have since been proposed [3]. However, due to hardware limitations, in particular the presence of enhanced carrier frequency offsets and DC offsets, the majority of these receivers saw little success.

Today, advances in radio frequency integrated circuit (RFIC) and in digital signal processing (DSP) capabilities allow for the correction of many of the architecture's historic drawbacks. With the ability to correct these traditional problems, the direct conversion architecture can provide a number of advantages over superheterodyne topology. Most notably, the single direct conversion to baseband allows all of the receiver filtering requirements for adjacent channels, blockers, and anti-aliasing filtering before sampling for digitization to be performed by a simple lowpass filter. [4]

Given these benefits, zero-IF receivers are increasingly being deployed across a wide range of applications. These include Bluetooth technology [5], mobile telephony and wireless local area network (LAN) applications [6], direct broadcast satellite [7], digital cable, and various broadand wireless metropolitan area network (MAN) applications [1].

1.2 Orthogonal Frequency Division Multiplexing

Broadband wireless applications are of particular interest in this work. Trends in broadband wireless communications systems are towards higher data rate capabilities and towards greater robustness in the face of typical wireless impairments such as frequency selective channels. Orthogonal frequency division multiplexing (OFDM)

is a form of multi-carrier modulation that provides an effective means of meeting these demands. It has consequently been adopted in a number of broadband wireless standards.

Much like the direct conversion architecture, the basic concept behind OFDM modulation is not new. Frequency Division Multiplexing (FDM) is a technique that combines multiple signals for simultaneous transmission over a single channel. Each signal is modulated with a simpler modulation scheme on a different carrier frequency within the channel. In a classical FDM system, there is no overlap between sub-channels in order to prevent Inter-Carrier Interference (ICI). Orthogonal Frequency Division Multiplexing (OFDM) is an evolution of this technique which arranges the sub-channels orthogonally such that their spectrums overlap without interfering with one another.

Proposed as early as 1967, this type of multiplexing was initially implemented with banks of filters and oscillators. Given the large number of devices that this would entail, OFDM did not see widespread use at the time. [8] However, current digital technologies have greatly simplified this process by enabling the use of Discrete Fourier Transform (DFT) and Inverse Discrete Fourier Transform (IDFT) for practical modulation and demodulation operations.

One of the major disadvantages of OFDM systems is high sensitivity to carrier frequency offset (CFO). The presence of CFO will result in the loss of orthogonality between OFDM sub-carriers, thereby causing significant inter-carrier interference (ICI) and performance degradation. Similarly, one of the major remaining problems for direct conversion receivers is the carrier frequency offset introduced in the down-conversion [4]. As such, the digital recovery of these offsets is an area of interest that merits closer examination for applications intending to combine the two technologies.

1.3 Carrier Frequency Offset Recovery

Various digital recovery techniques for carrier frequency offsets have been proposed. These techniques are seperated into two general classifications.

Traditional algorithms, classified as data-aided techniques, estimate and recover the CFO by inserting redundant data into the transmission. Common approaches involve reliance upon null tones [9], pilot tones [10], training sequences [11], or other redundant information that is inserted into the OFDM symbol [12] [13] [14]. Unfortunately, this use of redundant information reduces the maximum data throughput of a system.

Algorithms that estimate the carrier frequency offset without relying upon redundant data are classified as non-data-aided (more commonly referred to as blind) algorithms. Although a number of blind estimators have recently been advanced in the literature, [15] [12] [16] [17], most have a restricted set of operating conditions. For comparison, two of these blind approaches will be examined in greater detail herein.

An estimator based upon the correlation of specific samples in an OFDM symbol is presented by [15] and further explored by [12]. This estimator was designed with a flat channel in mind and consequently performs very poorly in frequency selective channels.

Another series of common CFO estimators are based upon exploiting the subspace structure of an OFDM symbol with super-resolution MUSIC-like [18] or ESPRIT-like [19] algorithms. Like other super-resolution algorithms, however, these estimators demonstrate poor performance below an SNR threshold which is relatively high.

1.4 Research Objectives

The objective of this thesis is to develop and to analyze an algorithm for blind CFO recovery suitable for use with a zero-IF OFDM telecommunications system. A mathematical model to characterize the algorithm's performance is to be derived and to be verified via simulation. Finally, the algorithm will be simulated under a selection of practical channel conditions and its performance will be compared to other blind algorithms in the literature.

As described above, some algorithms can only function within low noise or flat channels. Others have restrictions on frequency offset. The research objective is to develop a blind algorithm that recovers the carrier frequency offset in practical noisy and frequency selective channels. The algorithm should be capable of recovering the full range of possible carrier frequency offsets.

Standards like IEEE 802.16 [20] specify maximum tolerable post carrier recovery errors in the recovered carrier frequency. The variance or the mean squared error (MSE) is commonly used as the performand criterion for CFO estimators. This is the primary performance measure examined in this work.

A secondary performance measure examined is the number of symbols used to estimate the carrier frequency offset. This number is greatly effected by the presence or absence of a training sequence or pilot tones. A blind algorithm does not use a training sequence of pilot tones, so it does not require overhead on the transmitted data. Typically, blind CFO recovery techniques use a larger number of symbols than data-aided methods to get a CFO estimate with a similar variance. Given these constraints, the proposed algorithm will be designed around the type of long packet scenario. Additionally, the algorithm will be designed to operate without prior timing synchronization or channel equalization.

1.5 Thesis Organization

Background information relevant to understanding the problem, its context, and the proposed solution is presented in Chapter 2. First, an overview of the zero-IF architecture and its constraints for a digital recovery algorithm is provided. Second, a detailed explanation of OFDM principles and symbol characteristics is presented.

In Chapter 3, an algorithm for blind CFO recovery in a zero-IF OFDM system is proposed. As a foundation for the algorithm, the received signal's spectrum is examined, illustrating certain characteristics that can be leveraged to perform the blind carrier frequency offset recovery. This foundation is theoretically verified and the algorithm performance is analyzed.

Chapter 4 verifies the mathematics in Chapter 3 with simulation. Chapter 5 extends these simulations to provide practical performance results in a set of standard test channels. In order to evaluate the proposed algorithm's performance, the MSE of the CFO estimator is compared with that of other blind CFO estimators found in the literature. Finally, conclusions are presented in Chapter 6.

2. BACKGROUND INFORMATION

2.1 Receiver Architectures

Traditionally, digital communications receivers are divided into an analog and digital portion. The main function of the analog portion is to down-convert the signal to a frequency that can be sampled by a commercially available analog to digital converter (A/D). Virtually all of the signal processing is done in the digital domain. While the focus of this research primarily involves the development of DSP algorithms for carrier frequency offset recovery, the analog downconversion stage determines the nature of the input data and its impairments.

The following section compares the classical superheterodyne receiver architecture with that of a zero-IF receiver. This enables an appreciation of the advantages of the zero-IF receiver architecture which motivate its focus in this research. Furthermore, it allows for an understanding of the architecture's particular impairments that the research focuses on correcting.

2.1.1 Superheterodyne Receiver

The superheterodyne architecture, shown in Figure 2.1, is the most common receiver configuration in use today. The topology is based upon down-converting the received signal to some convenient intermediate frequency (IF). As is illustrated in the figure, the received signal first passes through a bandpass RF filter. This is a broadband filter whose purpose is to reduce the power in out-of-band signals that would otherwise cause the low-noise amplifier (LNA) to saturate.

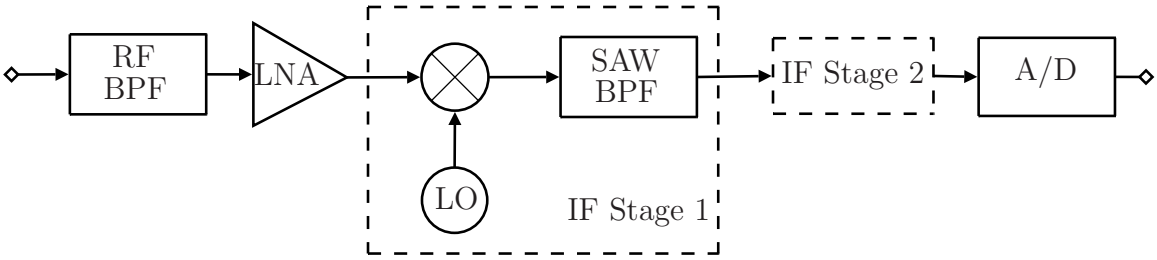

Figure 2.1: Superheterodyne receiver architecture

When the received signal is mixed with a local oscillator, both the desired IF signal and an undesirable image response are created as

$$f_{\text{IF}} = |f_c - f_{\text{LO}}| \tag{2.1}$$

$$f_{\text{image}} = \begin{cases} f_c + 2f_{\text{IF}} & ; f_{LO} > f_c \\ f_c - 2f_{\text{IF}} & ; f_{\text{LO}} < f_c \end{cases} \tag{2.2}$$

The intermediate frequency and the IF bandpass filter must have the following properties [2]

- The IF filter must provide steep attenuation outside the bandwidth of the IF signal in order to reject adjacent channels. This requires a sufficiently low IF that such a filter may be realized with practical components.
- The IF filter must reject the image response and other spurious responses from the mixer. This requires a sufficiently high IF that the two image frequencies are far enough apart.
- The intermediate frequency must be such that the previous criteria are met, and a stable high-gain IF amplifier can be economically implemented.

As carrier frequencies increase, many systems require multiple IF stages in cascade in order to sufficiently satisfy these criteria. Even then, these IF filters typically

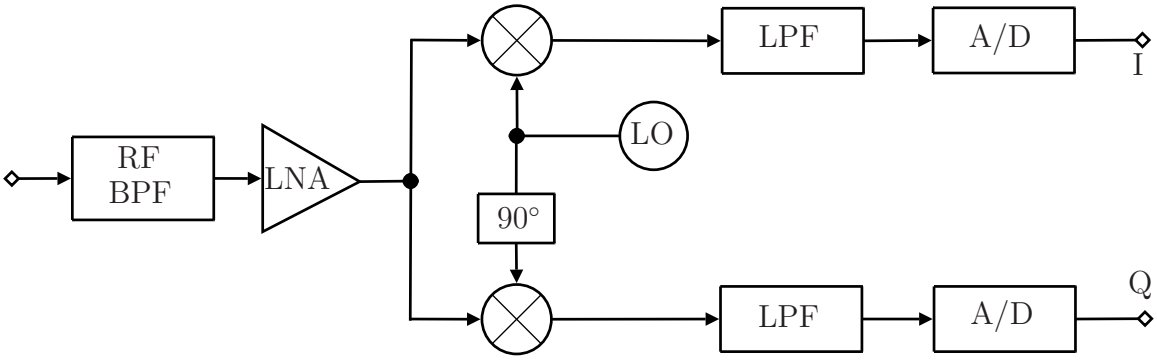

Figure 2.2: Zero-IF receiver architecture

require costly and bulky external filters such as surface acoustic wave (SAW) devices. [21] [22]

2.1.2 Zero-IF Receiver

The zero-IF receiver, also known as a homodyne, synchrodyne or direct conversion receiver, is a special case of the superheterodyne receiver that uses an LO with the same frequency as the carrier. In order for the detector to differentiate between signal components both above and below the LO frequency, zero IF receivers generate both In-Phase and Quadrature (IQ) signals. If the frequency band of interest has been translated directly to baseband, the IF filters are not required. Instead, low-pass filters can be used. The low-pass filters in the direct conversion receiver have lower power consumption, smaller size, higher reliability, greater ease of integration, and higher system flexibility than the IF filters used in the traditional superheterodyne.

The simplified RF front end makes the architecture of the direct conversion receiver attractive. However, there are design challenges. Care must be taken to ensure that the LO, which is at the frequency of the incoming signal, does not leak back through the front end mixer/amplifier/filter chain, which causes a DC offset. While a number of digital algorithms have recently been proposed to reduce or to eliminate

this DC offset, CFO recovery remains a challenge for the architecture.

2.2 Broadband Wireless Access

Broadband wireless metropolitan area networks (MAN) are highly complex communications systems. In order to ensure compatibility and to facilitate the interoperability of broadband wireless products from different manufacturers, experts in the field have collaborated to create a standardized air interface for fixed broadband wireless MANs. Known as IEEE 802.16 [20], the standard specifies the physical network layer which defines the transmission of data bits across a physical medium. This physical layer is based upon orthogonal frequency division multiplexing transmission scheme which is discussed in greater detail in Section 2.3. It also addresses other parameters such as transmission frequencies and bandwidths, wireless channel models, and synchronization requirements.

2.2.1 Wireless Channels

The physical transmission medium, known as the channel, is the air through which electromagnetic signals are broadcast. This channel is divided into generalized electromagnetic frequency bands. For example, IEEE 802.16 specifies the interface for licensed frequencies in the 2 to 11 GHz and the 10 to 66 GHz ranges. These bands are then further divided into segments with smaller bandwidths, known as sub-channels, that can be allocated for specific applications. For the purposes of this work, sub-channels 20 MHz wide with center frequencies in the 2 to 11 GHz range will be used.

When an electromagnetic signal is transmitted across a wireless channel, the terrain particularities will effect the received version of the signal. Environmental objects in and around the transmission path will change how a signal propagates. Instead

of receiving a single direct line-of-sight (LOS) signal, these objects create reflection, diffraction, and scattering effects that will introduce multiple delayed, attenuated, and phase shifted versions of that signal at the receiver. Combined, these effects are known as multipath. [23]

Mathematically, these channel effects act as a filter for the transmitted signal. In an ideal case where only the LOS signal is received, the magnitude of the frequency response of this filter is constant across the band. This is referred to as a flat channel. In the multipath case, the frequency response of the filter that models the channel is not constant. This is referred to as a frequency selective channel. In the IEEE 802.16 standard [20] and accompanying documents [24], IEEE 802.16 Task Group specify a series of standard multipath channel models for three general terrain types. This is explored in greater detail in Chapter 5.

2.3 Orthogonal Frequency Division Multiplexing

Orthogonal Frequency Division Multiplexing is an attractive multi-carrier modulation technique with the potential to provide high data rates and strong spectral efficiency in the face of multipath distortion.

OFDM takes an incoming bit stream and maps the bits to a series of amplitudes and phases with simpler modulation schemes. Each data mapping modulates one of N complex sinusoids. The frequency of these sinusoids is selected such that they are orthogonal to one another, thereby ensuring that their spectrums will overlap without interfering. As each complex sinusoid carries the modulated data at a specific baseband frequency, they are commonly referred to as sub-carriers.

Together, the sum of N modulated sub-carriers is referred to as an OFDM symbol. The duration of a symbol is equal to the period of its lowest frequency sinusoid.

During time, the phase and the amplitude modulation of the sub-carriers is held constant. Multiple symbols with different sets of modulation values are combined serially to form a baseband time domain signal. After some additional processing, this baseband signal is mixed with a local oscillator to an RF carrier frequency for transmission.

2.3.1 Orthogonality

One significant technical challenge for OFDM stems from its reliance on the orthogonality of the sub-carriers, which makes it very sensitive to carrier frequency offsets. Two signals, $x_1(t)$ and $x_2(t)$, are orthogonal to one another on a symbol interval, T, if:

$$\int_0^T x_1(t)x_2(t)dt = 0 \tag{2.3}$$

There are many ways to create orthogonal signals. Orthogonal Frequency Division Multiplexing uses an Inverse Fast Fourier Transform (IFFT). The IFFT is a computationally efficient algorithm to calculate the Inverse Discrete Fourier Transform (IDFT), which is given by

$$x(n) = \frac{1}{N}\sum_{k=0}^{N-1} X(\omega_k)e^{j\frac{2\pi kn}{N}}. \tag{2.4}$$

where N is the number of bins in the IFFT, $X(\omega_k)$ is the complex data mapping assigned to each bin, k is the index of each bin, and n is the sample index of the output time sequence. The number of bins in the IFFT is usually specified in standards like IEEE 802.16. The sampling points of the IFFT input bins are harmonically related with each bin at the frequency of a sub-carrier, i.e. $\omega_k = \omega_{\text{sub}}, 2\omega_{\text{sub}}, ..., k\omega_{\text{sub}}$ where ω_{sub} is the sub-carrier spacing.

For an OFDM system, the complex data mappings are given by $X(\omega_{\text{sub}}) = A_k e^{j\phi_k}$ hold the amplitude (A_n) and phase (ϕ_k) modulation information for each sub-carrier.

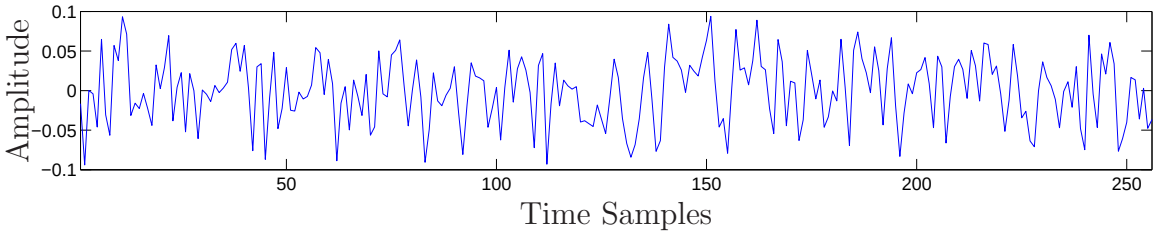

(a) Real component of a sample IFFT output time sequence

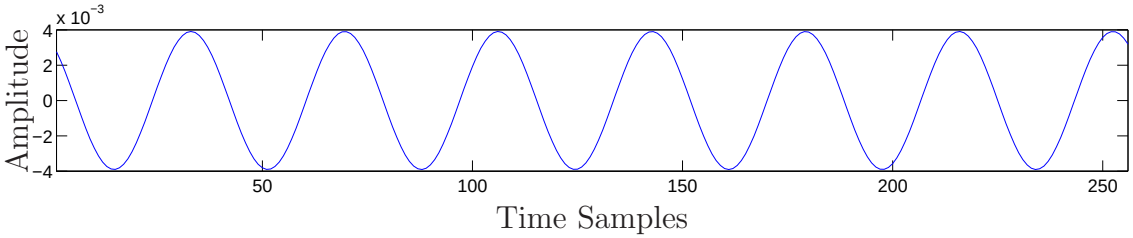

(b) Real component of the k^{th} harmonic of a sample IFFT output time sequence

Figure 2.3: Sample IFFT output time sequences

At the output of the IFFT, the resulting time sequence will be the sum of N orthogonal signals. Mathematically, this output can be expressed as

$$x(n) = \frac{1}{N} \sum_{k=1}^{N} x_k(n) \tag{2.5}$$

where each orthogonal signal is given by

$$x_1(n) = A_1 e^{j(\omega_{\text{sub}} n + \phi_1)} \tag{2.6}$$

$$x_2(n) = A_2 e^{j(2\omega_{\text{sub}} n + \phi_2)} \tag{2.7}$$

$$\vdots$$

$$x_k(n) = A_n e^{j(k\omega_{\text{sub}} n + \phi_k)}. \tag{2.8}$$

Figure 2.3(a) shows the real component of the IFFT output time sequence for an example set of mapped data, while Figure 2.3(b) shows the real component of the k^{th} harmonic of the IFFT output time sequence.

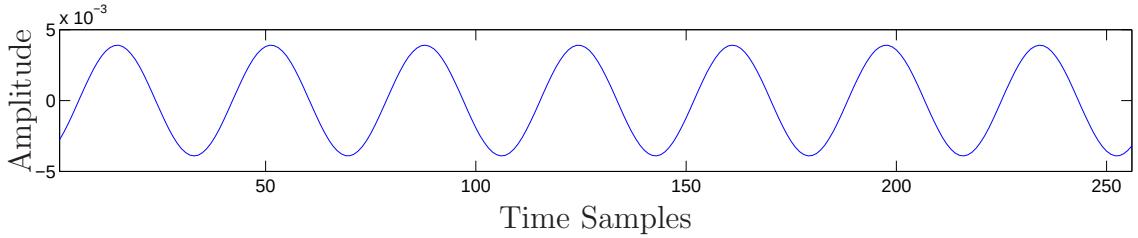

(a) Real component of a complex sinusoid that is orthogonal over the interval shown

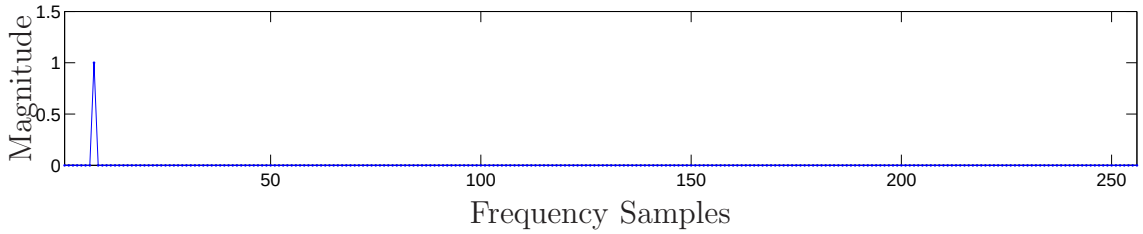

(b) Magnitude of the corresponding 256 sample FFT output

Figure 2.4: DFT results for an sinusoid that is orthogonal over the interval shown

When demodulating an OFDM signal at the receiver, the data mapping information is recovered by taking the Discrete Fourier Transform (DFT) of the received time sequence with the Fast Fourier Transform (FFT) algorithm. In order to retrieve the accurate data mapping information, it is critical that orthogonality is preserved. To illustrate this requirement, Figure 2.4(a) shows an uncorrupted sinusoid whose frequency is such that an integer number of cycles fit into the N sample FFT bin. Figure 2.4(b) shows the corresponding FFT output. At the peak of each harmonic, orthogonality ensures that there is no contribution from adjacent harmonics.

Unfortunately, several impairments can effect the orthogonality of the received signal. First, a bandlimiting filter is applied to the signal before transmission in order to limit out of band emissions. The impulse response of this filter causes interference from a delayed version of the tail end of the previously transmitted symbol. Similarly, a multipath channel introduces further cumulative delay. When taking the DFT of the resulting OFDM symbol in the demodulation process, the time sequence is no

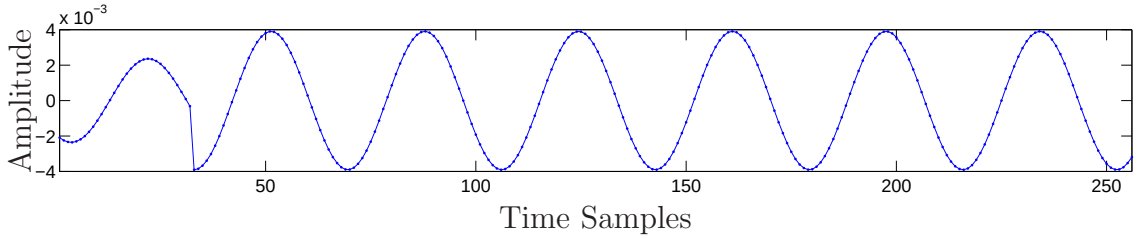

(a) Sinusoid whose start is corrupted with delayed samples from a previous symbol

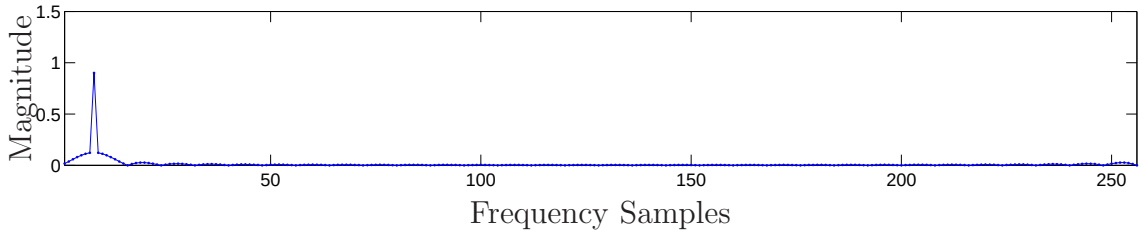

(b) Magnitude of the corresponding 256 sample FFT output

Figure 2.5: DFT results for an sinusoid with delayed samples from a previous symbol

longer orthogonal over the interval N. This is illustrated in Figure 2.5. Figure 2.5(a) shows N samples from a sinusoidal input to the FFT that experiences Inter-Symbol Interference (ISI). Figure 2.5(b) shows the magnitude of the corresponding FFT output result. The non-zero contribution from this harmonic in adjacent bins makes it much more difficult to decide what data mapping was transmitted.

In order to combat this Inter-Symbol Interference, Orthogonal Frequency Division Multiplexing uses a cyclic prefix before each symbol. A number of samples, which will be denoted N_{CP}, from the tail end of a symbol are copied and are pre-appended at the beginning of the symbol. N_{CP} is chosen to be large enough to hold all of the ISI created by the filtering and by the channel. This allows the demodulator to select N samples from the symbol that do not experience ISI for use in the DFT.

Another impairment that destroys the orthogonality of an OFDM symbol is the carrier frequency offset. CFO will introduce a frequency shift in the received baseband signal. When the frequency of the harmonics $x_k(n)$ is such that an integer number

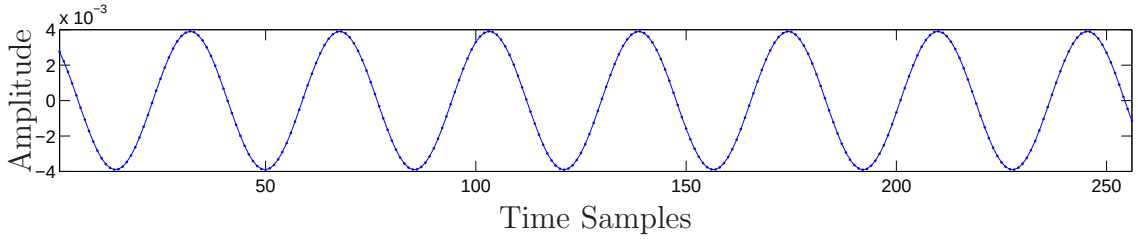

(a) Sinusoid with carrier frequency offset

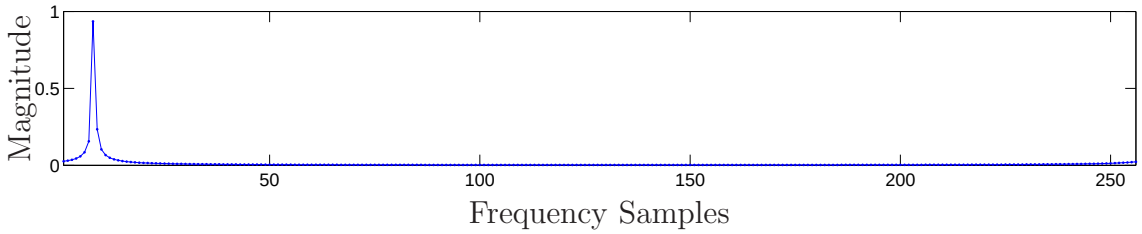

(b) Magnitude of the corresponding 256 sample FFT output

Figure 2.6: DFT results for an sinusoid that is not orthogonal over the interval shown

of cycles does not fit into the interval N, orthogonality is lost and the FFT result from each sub-carrier will be non-zero in adjacent frequency bins. This impairment, known as Inter-Carrier Interference (ICI), is illustrated in Figure 2.6.

Figure 2.6(a) shows a sinusoid with a small frequency offset such that it does not have an integer number of cycles over the interval N. Figure 2.6(b) shows the magnitude of the resulting FFT output which experiences ICI. The goal of this work is to prevent this ICI by recovering the carrier frequency offset of the baseband received signal.

2.3.2 OFDM Transmitter Model and Symbol Construction

Having outlined the theoretical basis of Orthogonal Frequency Division Multiplexing, the specific format of OFDM symbols pertinent to this research can now be discussed. As a reference point for this discussion, Figure 2.7 illustrates the system model of a generalized OFDM transmitter. The transmitter signal path begins with

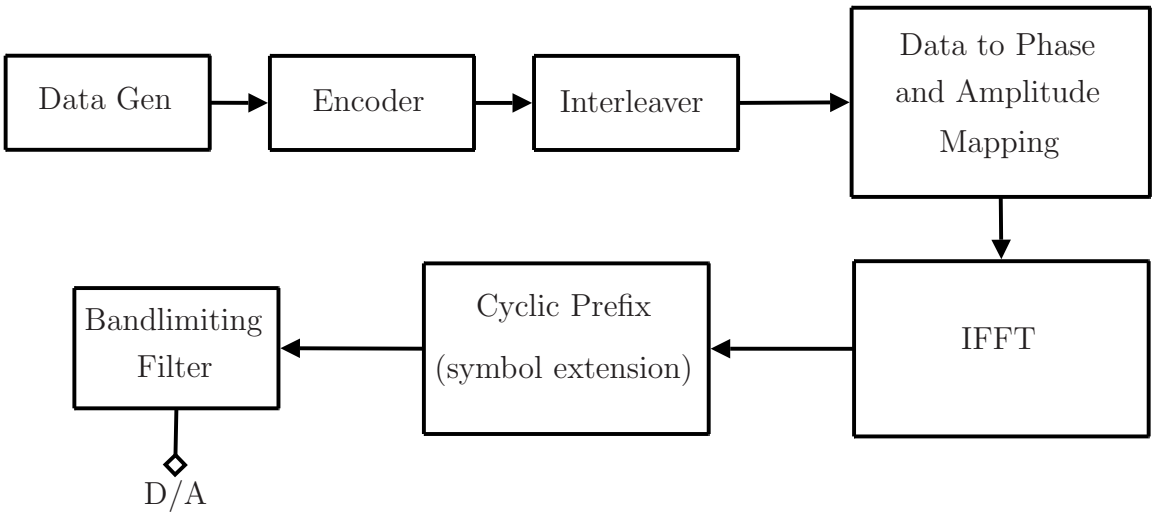

Figure 2.7: OFDM transmitter block diagram

the data generation, coding, and interleaving. These steps do not impact the proposed frequency offset recovery process and are not discussed. Following coding and interleaving, the data is mapped to phases and amplitudes of the sub-carriers, transformed with an IFFT, and extended with a cyclic prefix. It is then filtered and sent to a digital to analog converter (D/A) after which it is translated and transmitted by the analog RF circuit.

Sub-carrier Modulation

Depending upon the specific application, a wide range of modulation schemes can be applied to OFDM sub-carriers. Within the IEEE 802.16 broadband wireless standard, a number of Phase Shift Keying (PSK) and Quadrature Amplitude Modulation (QAM) schemes are supported.

In Phase Shift Keying, the input data is modulated by changing the phase of the complex sub-carrier. The simplest case of PSK is Binary Phase Shift Keying (BPSK) which has two possible phases separated by 180°. In order to make use of both I and

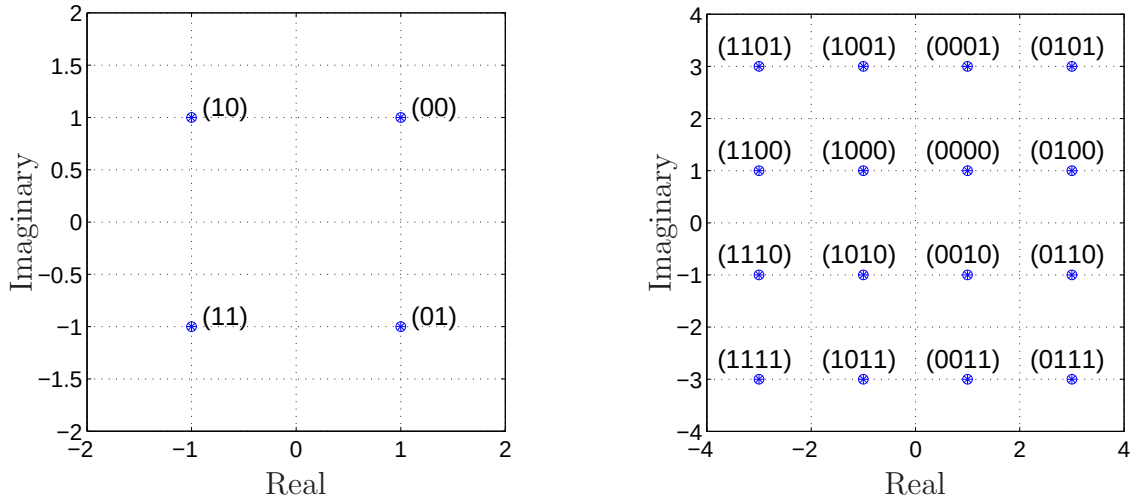

(a) QPSK constellation

(b) Rectangular 16-QAM constellations

Figure 2.8: Gray mapped QPSK and rectangular 16-QAM constellations

Q components of a complex sub-carrier, it is common to alternately map BPSK along the I and Q axes of the unit circle. This is known as spread-BPSK.

The next step up in complexity is Quadrature Phase Shift Keying (QPSK) modulation. This scheme maps two bits of data to one of four possible phases that are equally spaced around the unit circle. While a number of methods for mapping the bits to their respective phases are possible, the IEEE 802.16 standard specifies the common Gray Mapping as is illustrated in the constellation shown in Figure 2.8(a).

In Quadrature Amplitude Modulation, the input data is modulated by changing the amplitudes of the I and Q components of the complex sub-carriers. While the previous two modulation schemes can be viewed as special cases of QAM, this method is typically associated with a higher number of possible symbols in its constellation. For an M-QAM scheme, k bits are mapped into one of M possible symbols, where $M = 2^k$. A large number of possible constellations are possible. Rectangular constellations have well defined demodulation decision boundaries. Given the ease of implementing

these decision boundaries, rectangular constellations find popular use. Figure 2.8(b) shows an example Gray Mapped 16-QAM constellation as specified on page 330 of the IEEE 802.16 standard [20].

Inverse Fast Fourier Transformation

Once an incoming bit stream has successfully been mapped to a series of complex phases and amplitudes as described above, an overall symbol can be formed by modulating N orthogonal sinusoidal sub-carriers with N data mappings. Typically, this is performed via an Inverse Fast Fourier Transform operation.

At this stage, many applications, specifications, and standards insert pilot symbols at regular intervals between the mapped data. These pilots are redundant data with a known amplitude and phase that are used for various functions within a receiver. For example, they can be used to equalize the channel. They can also be used to facilitate frequency recovery.

Additionally, nulls are also commonly inserted into the spectrum before the IFFT. Though nulls are special pilots with a value of zero, they are included for different reasons than standard pilots. A null at DC is often included to allow for the correction of DC offsets introduced by local oscillator feed through in the zero-IF downconversion process. A series of nulls at the band edges are also commonly included to form guard bands to help limit out-of-band emissions for transmission.

As the goal of this research is to produce a blind CFO recovery algorithm, pilot tones will not be used. Similarly, nulls will only be used to provide guard bands to limit out of band emissions or to combat the zero-IF DC offset design challenge. As specified in the IEEE 802.16 standard, 256 sub-carriers are used in the IFFT to create each OFDM symbol. Of these, 200 sub-carriers hold modulated data andr the

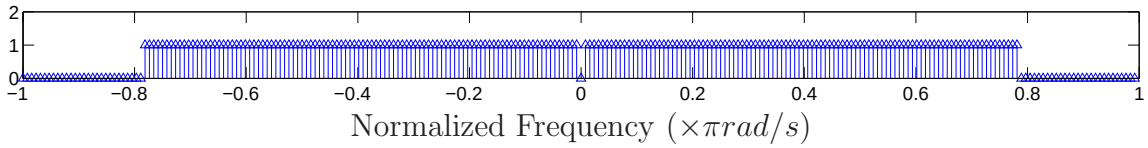

Figure 2.9: OFDM message symbol spectral arrangement

remainder are null sub-carriers. Figure 2.9 illustrates the spectral arrangement of an example OFDM symbol used in the later portions of this research.

Cyclic Prefix Extension

As described in Section 2.3.1, a cyclic prefix extension of the message symbol is used to combat Inter-Symbol Interference from the combined delays of filtering and transmission through a multipath channel.

Practically speaking, the delay of multipath signals with sufficient strength to interfere with subsequently received LOS signals is usually significantly less than one symbol duration. Similarly, band-limiting filters typically have short impulse responses. As such, a number of samples from the end of the symbol are pre-appended to the front of the symbol to create a cyclic prefix buffer to absorb potential ISI.

When selecting the length of a the cyclic prefix, some knowledge of the expected channel characteristics is required. For this purpose, a number of commonly used multipath channel models have been proposed [24] for the IEEE 802.16 standard. Based on these models, the standards are designed with a set of three pre-determined prefix lengths. Specifically, the cyclic prefix can be 16, 32, or 64 samples long. These lengths can either be selected at device initialization, or more advanced applications can switch between the specified options as channel conditions change.

2.4 Carrier Frequency Offset

OFDM's reliance on the orthogonality between sub-carriers makes it very sensitive to carrier frequency offsets. A small frequency shift in the received signal will mean that the sub-carriers are no longer located at integer multiples of the sub-carrier spacing. As such, the demodulated signal will experience inter-carrier interference (ICI) which will degrade the system performance if these offsets are not appropriately recovered.

In practical systems, carrier frequency offsets are introduced by doppler shifts and by physical differences between the LO crystals in the transmitter and the receiver. Offsets introduced by the latter can be quite substantial. For example, a crystal tolerance of 100ppm in a 5 GHz oscillator could have a frequency offset of up to 500 kHz. In IEEE 802.16a, center frequencies range from 2 MHz to 11 MHz with 256 sub-carriers spaced across a band 20 MHz wide. Clearly, the carrier frequency offset can often be greater than the spacing between sub-carriers.

The problem of carrier frequency offset recovery is therefore broken into a coarse and a fine stage. When the CFO is greater than half of the spacing between sub-carriers, which is generally true, an initial coarse estimate is used to determine the portion of the CFO that is an integer number of sub-carrier spacings. A number of well-established and straightforward algorithms exist to perform this coarse estimation [25], and this stage will therefore not be explored in detail herein. The second stage of CFO recovery, which the proposed algorithm addresses, aims to recover the fine portion of the CFO that is within plus or minus one-half of the sub-carrier spacing.

3. ALGORITHM AND ANALYSIS

In this section, an algorithm for blind CFO recovery in a zero-IF OFDM system is proposed. The power spectrum of a received OFDM signal is analyzed, revealing a raised sinusoidal characteristic in the the signal's passband. This characteristic shape can be harnessed to recover the carrier frequency offset without requiring the addition of any redundant data. The specific algorithm details to accomplish this are described and the algorithm's expected performance is analyzed.

3.1 Power Spectrum Analysis

The shape of received signal's power spectrum provides the foundation for the proposed algorithm. A general OFDM symbol consists of N modulated sub-carriers which, at baseband, can be expressed by the complex signal:

$$x(n) = \frac{1}{N} \sum_{i=-\frac{N}{2}}^{\frac{N}{2}-1} A_i e^{j\left(i\omega_{\text{sub}} n + \Delta\omega n + \phi_i(n)\right)}; 0 \leq n < N + N_{CP} \tag{3.1}$$

where ω_{sub} is the frequency spacing between adjacent sub-carriers, $\Delta\omega$ is the carrier frequency offset, A_i is the amplitude of the i^{th} subcarrier, and $\phi_i(n)$ is the phase of the i^{th} subcarrier. The symbol duration is $N + N_{CP}$ samples where N is the length of the IFFT used in the symbol construction and N_{CP} is the length of the cyclic prefix. In a typical system, the majority of sub-carriers will be modulated by data, while a smaller number will be pilot or null sub-carriers that are either transmitted with a known phase and amplitude, or are not transmitted at all, respectively. For the purposes of this discussion, all sub-carriers will be treated as data-modulated carriers.

The power spectrum, $S_{xx}(k)$, of this OFDM symbol is given by

$$S_{xx}(k) = E[X(k)X^*(k)], \tag{3.2}$$

where $X(k)$ is the DFT of the received OFDM signal, and $X^*(k)$ is its complex conjugate. The length of the DFT used in computing $X(k)$ and $X^*(k)$ will determine the frequency resolution of the resulting power spectrum $S_{xx}(k)$. Initial analysis is based upon a DFT length of $2N$ samples which includes parts of two adjacent symbols. The DFT is given by

$$X(k) = \frac{1}{N} \sum_{n=0}^{2N-1} \sum_{i=-\frac{N}{2}}^{\frac{N}{2}-1} A_i e^{\frac{j2\pi in}{N}} e^{j\phi_i(n)} e^{j\frac{2\pi kn}{2N}} e^{j\Delta\omega n} \tag{3.3}$$

and the conjugate of $X(k)$ is given by

$$X^*(k) = \frac{1}{N} \sum_{m=0}^{2N-1} \sum_{l=-\frac{N}{2}}^{\frac{N}{2}-1} A_l e^{\frac{-j2\pi lm}{N}} e^{-j\phi_l(m)} e^{-j\frac{2\pi km}{2N}} e^{-j\Delta\omega n} \tag{3.4}$$

where the indices i and l and n and m are used in preparation for expressing the product $X(k)X^*(k)$ as a quadruple sum. Specifically, n and m are the indices for the $2N$ point DFT, while i and l are the indices for each sub-carrier in the ODFM symbols.

The power spectrum can be expressed as the quadruple sum,

$$S_{xx}(k) = E\left[\frac{1}{N^2} \sum_{m=0}^{2N-1} \sum_{l=-\frac{N}{2}}^{\frac{N}{2}-1} \sum_{n=0}^{2N-1} \sum_{i=-\frac{N}{2}}^{\frac{N}{2}-1} A_i A_l e^{j(\phi_i(n)-\phi_l(m))} e^{j\frac{2\pi}{N}(in-lm)} e^{j\frac{2\pi k}{2N}(n-m)} e^{j\Delta\omega(n-m)}\right]. \tag{3.5}$$

Within this expectation, the data modulation is the only random quantity. As such, the expectation operation can be brought in to produce,

$$S_{xx}(k) = \frac{1}{N^2} \sum_{m=0}^{2N-1} \sum_{l=-\frac{N}{2}}^{\frac{N}{2}-1} \sum_{n=0}^{2N-1} \sum_{i=-\frac{N}{2}}^{\frac{N}{2}-1} E\left[A_i A_l e^{j(\phi_i(n)-\phi_l(m))}\right] e^{j\frac{2\pi}{N}(in-lm)} e^{j\frac{2\pi k}{2N}(n-m)} e^{j\Delta\omega(n-m)}. \tag{3.6}$$

Since standard transmitters virtually always include a randomizer to ensure data independence, the data modulating different sub-carriers is assumed to be independent,

$$E\left[A_i A_l e^{j\phi_i(m)} e^{-j\phi_l(m)}\right] = 0 \text{ if } i \neq l. \tag{3.7}$$

As such, the summation over i and l reduces to a single summation over i. The reduced expression for the power spectrum is given by,

$$S_{xx}(k) = \frac{1}{N^2} \sum_{m=0}^{2N-1} \sum_{n=0}^{2N-1} \sum_{i=-\frac{N}{2}}^{\frac{N}{2}-1} E\left[A_i^2 e^{j(\phi_i(n)-\phi_i(m))}\right] e^{j\frac{2\pi i}{N}(n-m)} e^{j\frac{2\pi k}{2N}(n-m)} e^{j\Delta\omega(n-m)}. \tag{3.8}$$

The amplitude A_i is independent from the phase $e^{j\phi_i(n)}$ for every i and for any n or m. As such, the product $E\left[A_i^2 e^{j(\phi_i(n)-\phi_i(m))}\right]$ can be separated to $E[A_i^2]E\left[e^{j(\phi_i(n)-\phi_i(m))}\right]$. This allows (3.8) to be re-written as

$$S_{xx}(k) = \frac{1}{N^2} \sum_{m=0}^{2N-1} \sum_{n=0}^{2N-1} \sum_{i=-\frac{N}{2}}^{\frac{N}{2}-1} E[A_i^2] E\left[e^{j(\phi_i(n)-\phi_i(m))}\right] e^{j\frac{2\pi i}{N}(n-m)} e^{j\frac{2\pi k}{2N}(n-m)} e^{j\Delta\omega(n-m)} \tag{3.9}$$

A triangular function, $\wedge_M(\lambda)$, may be defined as:

$$\wedge_M(\lambda) = \begin{cases} \frac{M-|\lambda|}{M} & ; |\lambda| < M \\ 0 & ; \text{otherwise} \end{cases} \tag{3.10}$$

The modulation of each OFDM symbol is constant over the symbol's duration of $N + N_{CP}$ samples, and the modulations of adjacent symbols are independent. For an arbitrary time origin, the boundary between the two symbols is arbitrary and $e^{j(\phi_i(n)-\phi_i(m))}$ is a stationary process. Therefore, its expected value is a triangle

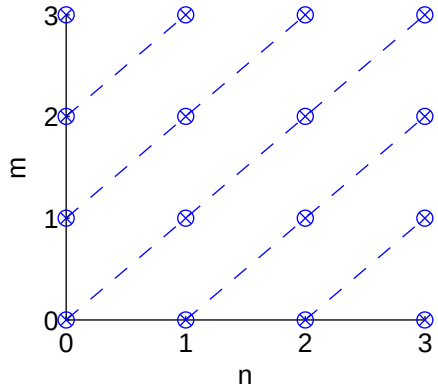

Figure 3.1: Illustration of the simplification of a double sum

function given by

$$E\left[e^{j(\phi_i(n)-\phi_i(m))}\right] = \wedge_{N+N_{CP}}(n-m)$$
$$= \begin{cases} \frac{N+N_{CP}-|n-m|}{N+N_{CP}} & |n-m| < N+N_{CP} \\ 0 & \text{otherwise} \end{cases} \tag{3.11}$$

For notational convenience, the inner sum on the right hand side of Equation (3.9) is represented by $g_k(n-m)$.

$$g_k(n-m) = \frac{1}{N^2} \sum_{i=-\frac{N}{2}}^{\frac{N}{2}-1} E\left[A_i^2\right] E\left[e^{j(\phi_i(n)-\phi_i(m))}\right] e^{j\frac{2\pi i}{N}(n-m)} e^{j\frac{2\pi k}{2N}(n-m)} e^{j\Delta\omega(n-m)} \tag{3.12}$$

Making the substitution, (3.9) becomes,

$$S_{xx}(k) = \frac{1}{N^2} \sum_{m=0}^{2N-1} \sum_{n=0}^{2N-1} g_k(n-m) \tag{3.13}$$

The double summation over n and m in Equation (3.13) can be transformed into a single summation. This transformation is illustrated in Figure 3.1, which identifies the values of $g_k(n-m)$ that are the same by linking them with a dashed line. Taking

advantage of this reduces the double sum to a single sum as follows

$$\sum_{m=0}^{2N-1}\sum_{n=0}^{2N-1} g_k(n-m) = \sum_{\lambda=-(2N-1)}^{2N-1} (2N-|\lambda|)g_k(\lambda)$$
$$= \sum_{\lambda=-(2N-1)}^{2N-1} 2N \wedge_{2N}(\lambda) g_k(\lambda) \tag{3.14}$$

where $\lambda = n - m$. The power spectrum becomes:

$$S_{xx}(k) = \frac{1}{N^2} \sum_{\lambda=-(2N-1)}^{2N-1} 2N \wedge_{2N}(\lambda) e^{j\frac{2\pi k}{2N}\lambda} e^{j\Delta\omega\lambda} \wedge_{N+N_{CP}}(\lambda) \sum_{i=-\frac{N}{2}}^{\frac{N}{2}-1} E\left[A_i^2\right] e^{j\frac{2\pi i}{N}\lambda} \tag{3.15}$$

Without loss of generality, the expected value of A_i^2 is taken to be a constant value of 1 for all i. In practical systems, the length of the cyclic prefix is less than N so that $N + N_{CP} < 2N$. The triangle function $\wedge_{N+N_{CP}}(\lambda)$ will be zero for $|\lambda| \geq N + N_{CP}$. This means that the limits of λ for the outer summation in (3.15) can be reduced to $\pm(N + N_{CP})$ and the power spectrum becomes:

$$S_{xx}(k) = \frac{1}{N^2} \sum_{\lambda=-(N+N_{CP})}^{N+N_{CP}} 2N \wedge_{2N}(\lambda) e^{j\frac{2\pi k}{2N}\lambda} e^{j\Delta\omega\lambda} \wedge_{N+N_{CP}}(\lambda) \sum_{i=-\frac{N}{2}}^{\frac{N}{2}-1} e^{j\frac{2\pi i}{N}\lambda} \tag{3.16}$$

Using the geometric progression [26]

$$\sum_{i=-\frac{N}{2}}^{\frac{N}{2}-1} a^i = \begin{cases} \dfrac{a^{-\frac{N}{2}} - a^{\frac{N}{2}}}{1-a} & ; a \neq 1 \\ N & ; a = 1 \end{cases}, \tag{3.17}$$

the inner sum evaluates to

$$\sum_{i=-\frac{N}{2}}^{\frac{N}{2}-1} e^{j\frac{2\pi i}{N}\lambda} = \begin{cases} N & ; \lambda = -N, 0, N \\ 0 & ; \text{otherwise} \end{cases} \tag{3.18}$$

Substituting (3.18) into (3.16) provides,

$$\begin{aligned} S_{xx}(k) = \; & 2 \wedge_{2N}(-N) \wedge_{N+N_CP}(-N) e^{-j\pi k} e^{-j\Delta\omega N} \\ & +2 \wedge_{2N}(0) \wedge_{N+N_CP}(0) \\ & +2 \wedge_{2N}(N) \wedge_{N+N_CP}(N) e^{j\pi k} e^{j\Delta\omega N} \\ = \; & 2\left[1 + \frac{2N-N}{2N}\frac{N+N_{CP}-N}{N+N_{CP}}\left(e^{j(\pi k+\Delta\omega N)} + e^{-j(\pi k+\Delta\omega N)}\right)\right] \\ = \; & 2\left[1 + \frac{N_{CP}}{N+N_{CP}}\cos(\pi k + \Delta\omega N)\right] \end{aligned} \tag{3.19}$$

Equation (3.19) indicates that the power spectrum of a $2N$ segment of an OFDM signal is a raised sinusoid. The magnitude of the sinusoidal component varies based on the length of the cyclic prefix. The sinusoidal component has a period of one sub-carrier spacing and has a phase such that its peaks occur at the frequency locations of the OFDM sub-carriers when there is no carrier frequency offset. This is illustrated in Figure 3.2. As there are many sub-carriers within the spectrum, only a zoomed in section of the spectrum is shown in Figure 3.2. Note that neither the x or y axes begin at the origin in the section shown.

A carrier frequency offset, introduced by imperfect downconversion, shifts the phase of the sinusoidal component. For example, if the local oscillator in the zero-IF downconverter has a frequency error of $0.35\omega_{\text{sub}}$, the power spectrum of the baseband signal is shown in Figure 3.3.

3.1.1 Generalized Length Power Spectrum Analysis

If a greater frequency resolution is required, the analysis can be extended from a DFT length of $2N$ to one of αN for α an integer. With a DFT length of αN samples, the analysis is similar, and what follows is somewhat repetitious.

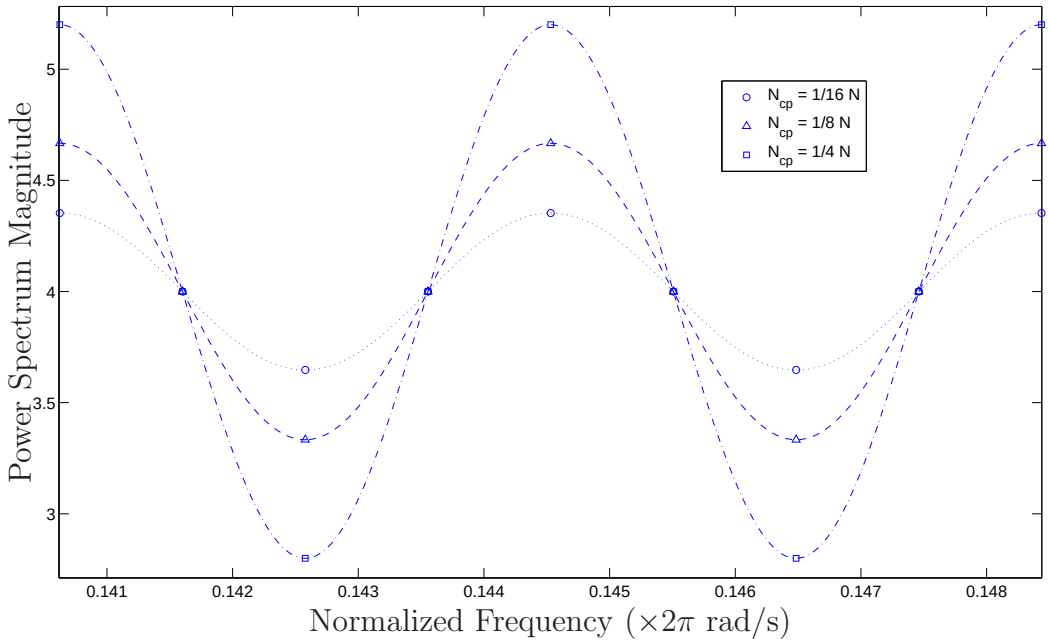

Figure 3.2: Theoretical power spectrum with varied cyclic prefix length

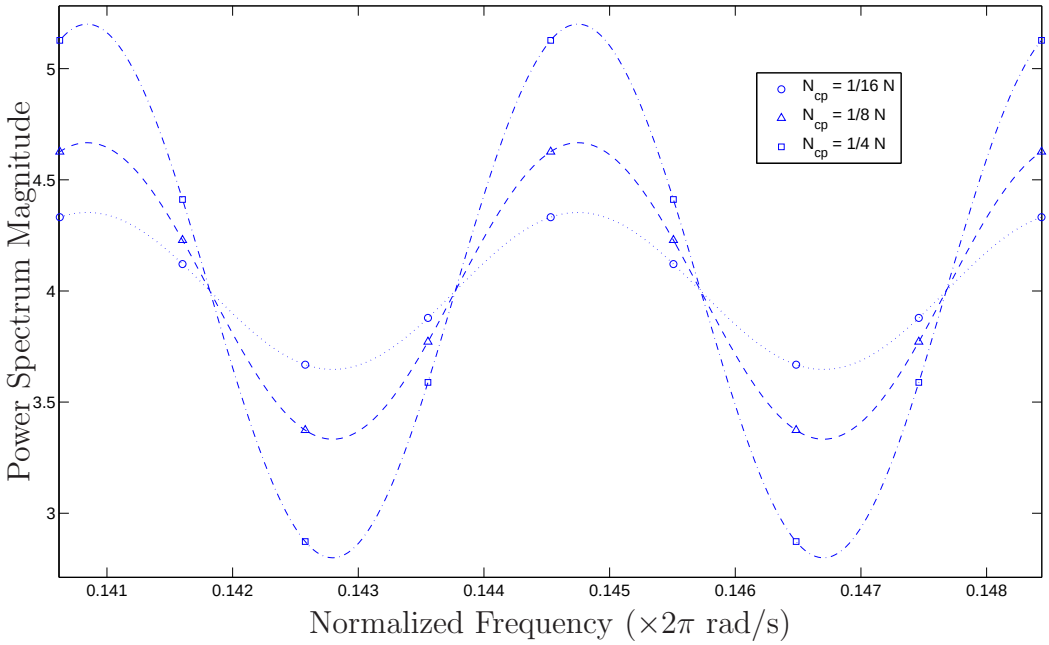

Figure 3.3: Theoretical power spectrum with varied cyclic prefix length and CFO

$$S_{xx}(k) = \frac{1}{N^2} \sum_{m=0}^{\alpha N-1} \sum_{n=0}^{\alpha N-1} \sum_{i=-\frac{N}{2}}^{\frac{N}{2}-1} \wedge_{N+N_{CP}}(n-m) e^{j\frac{2\pi i}{N}(n-m)} e^{j\frac{2\pi k}{\alpha N}(n-m)} e^{j\Delta\omega(n-m)} \quad (3.20)$$

The double sum is simplified as before to:

$$\begin{aligned} \sum_{m=0}^{\alpha N-1} \sum_{n=0}^{\alpha N-1} g_k(n-m) &= \sum_{\lambda=-(\alpha N-1)}^{\alpha N-1} (\alpha N - |\lambda|) g_k(\lambda) \\ &= \sum_{\lambda=-(\alpha N-1)}^{\alpha N-1} \alpha N \wedge_{\alpha N}(\lambda) g_k(\lambda) \end{aligned} \quad (3.21)$$

As with the $\alpha = 2$ case, the range of λ is again constrained to $|\lambda| \leq N + N_{CP}$ where $N + N_{CP} < 2N$. Therefore, the limits in the outer sum can be reduced to get:

$$S_{xx}(k) = \frac{1}{N^2} \sum_{\lambda=-(N+N_{CP})}^{N+N_{CP}} \alpha N \wedge_{\alpha N}(\lambda) e^{j\frac{2\pi k}{\alpha N}\lambda} e^{j\Delta\omega\lambda)} \wedge_{N+N_{CP}}(\lambda) \sum_{i=-\frac{N}{2}}^{\frac{N}{2}-1} e^{j\frac{2\pi i}{N}\lambda} \quad (3.22)$$

The inner sum is again zero for all values of λ except for $\lambda = -N, 0, N$ with the same rationale as in (3.18). Therefore, the generalized power spectrum can be expressed as:

$$\begin{aligned} S_{xx}(k) = \; & \alpha \wedge_{\alpha N}(N) \wedge_{N+N_CP}(N) e^{j\frac{2\pi}{\alpha}k} e^{j\Delta\omega N} \\ & + \alpha \wedge_{\alpha N}(0) \wedge_{N+N_CP}(0) \\ & + \alpha \wedge_{\alpha N}(-N) \wedge_{N+N_CP}(-N) e^{-j\frac{2\pi}{\alpha}k} e^{-j\Delta\omega N} \\ = \; & \alpha \left[1 + \frac{\alpha N - N}{\alpha N} \frac{N + N_{CP} - N}{N + N_{CP}} \left(e^{j(\frac{2\pi}{\alpha}k + \Delta\omega N)} + e^{-j(\frac{2\pi}{\alpha}k + \Delta\omega N)} \right) \right] \\ = \; & \alpha \left[1 + \frac{\alpha - 1}{\alpha} \frac{N_{CP}}{N + N_{CP}} 2\cos\left(\frac{2\pi}{\alpha}k + \Delta\omega N \right) \right] \end{aligned} \quad (3.23)$$

As before, Equation (3.23) shows that the power spectrum of an αN segment of an OFDM signal is a raised sinusoid with a phase that is proportional to the carrier frequency offset. The sinusoidal component has a period of one sub-carrier spacing with α samples per period. The magnitude of the sinusoid relative to its DC offset

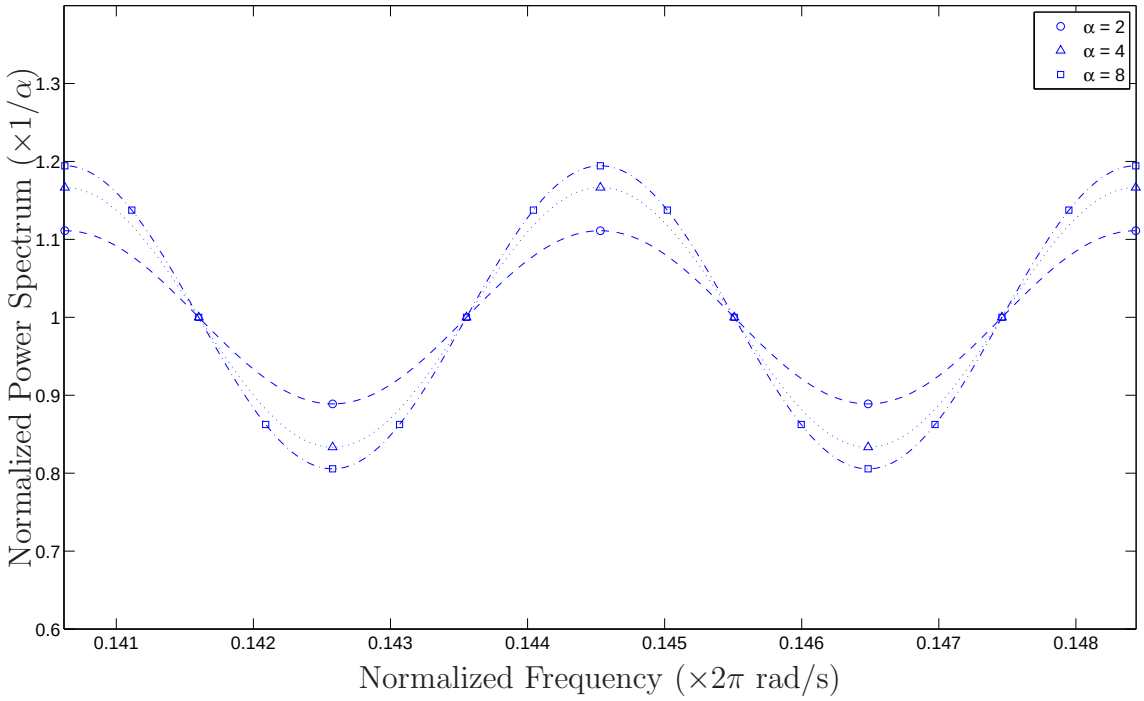

Figure 3.4: Theoretical power spectrum with DFT length α varied

changes with α as well as with N_{CP}, although the former has significantly less impact. Figure 3.4 present a series of power spectral densities with α varied. In this case, the magnitudes of the power spectrums are normalized by alpha in order to compare the results with a constant mean.

3.2 Algorithm Description

3.2.1 Overview and Block Diagram

The proposed recovery algorithm has a relatively simple feed-forward structure. It can be described with three blocks as shown in Figure 3.5.

The first block in Figure 3.5, estimates the power spectrum of the received signal. The power spectrum is partitioned into two areas as shown in Figure 3.6. One is

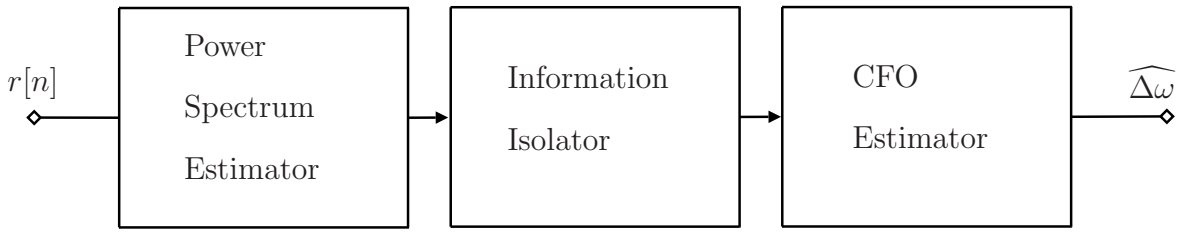

Figure 3.5: Overall block diagram of proposed CFO estimator

denoted the information portion and the other is called the guard band. The information portion is spectrum where there are data-bearing sub-carriers and the guard band portion is spectrum there are null sub-carriers. The power spectrum estimator allows the algorithm to take advantage of the raised sinusoidal component in the information portion of the spectrum.

The second block in Figure 3.5 therefore extracts the information portion of the power spectrum, which is a raised sinusoid. The period of this sinusoid is dependent on system parameters, and its phase is proportional to the carrier frequency offset. The third block in Figure 3.5 estimates the phase of this sinusoid with Fourier series coefficients. It then converts this to an estimate of the carrier frequency offset with a simple scaling factor.

The following sections examine each block in greater detail.

3.2.2 Power Spectrum Estimator

There are many digital signal processing techniques that can be used to estimate a signal's power spectrum [27]. The estimation method used in this algorithm is shown in Figure 3.7.

As data arrives at the receiver, the received time-domain signal is segmented into blocks of data as illustrated in Figure 3.8. These data segments are not synchronized

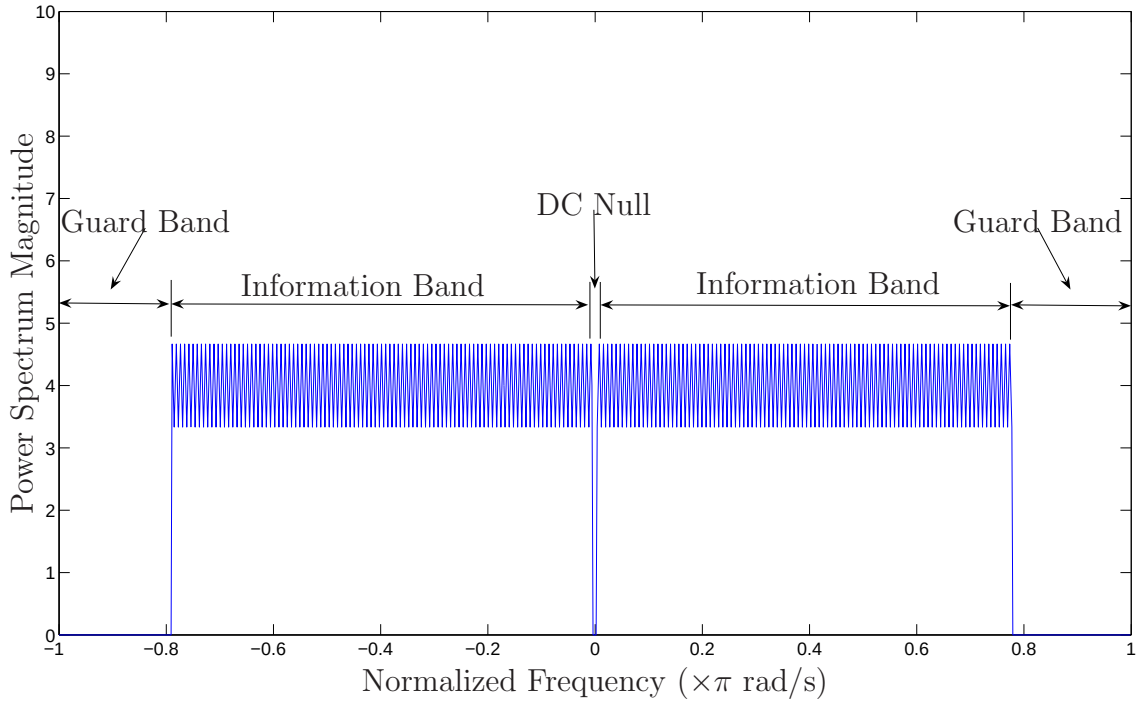

Figure 3.6: Power spectrum partitioning

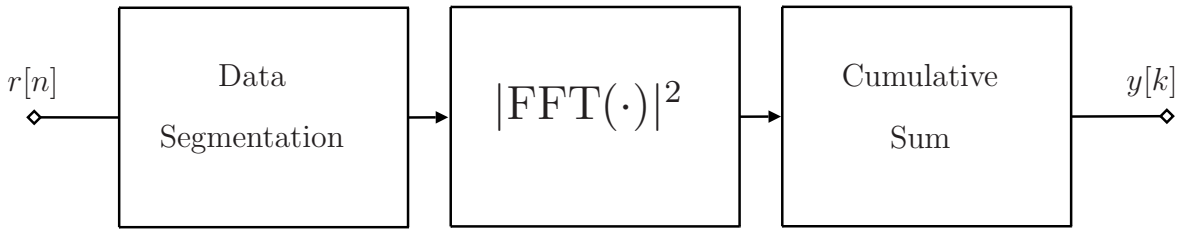

Figure 3.7: Block diagram of power spectrum estimator

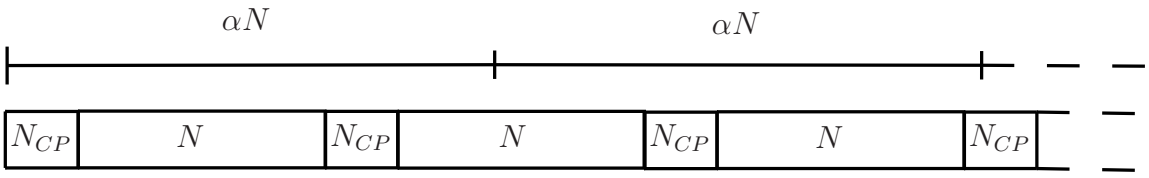

Figure 3.8: Illustration of data segmentation

to a symbol boundary. The collection window for each segment is αN samples, where α is an integer. Each received data symbol, on the other hand, has a length of $N + N_{\mathrm{CP}}$. Figure 3.8 illustrates this segmentation for $\alpha = 2$.

The Fast Fourier Transform (FFT) is then computed for each data segment. The FFT transforms a finite input sequence into its frequency components. The resulting sequence is a sampled representation of the frequency domain. The magnitude squared of this resulting sequence is an estimate of the input signal's power spectrum.

Figure 3.9(a) shows the continuous power spectrum of an OFDM signal. The period of the sinusoidal component in this spectrum is equal to the OFDM sub-carrier spacing. When the power spectrum is estimated with a finite length FFT, the period of the observed raised sinusoid remains equal to this sub-carrier spacing. However, this FFT produces a sampled spectrum with a number of samples equal to its input segment length. Specifically, when the power spectrum of an OFDM signal with N sub-carriers is estimated with an FFT of length αN, the resulting estimate has α samples per sub-carrier spacing. Since the period of the sinusoidal component is one sub-carrier spacing, there are α samples per period of the sinusoidal component. Figures 3.9(b) and (c) show the sampled power spectrum for $\alpha = 2$ and $\alpha = 4$, respectively.

When roughly estimating the power spectrum as the magnitude squared of the FFT, the variance of the estimate at a given frequency does not significantly decrease

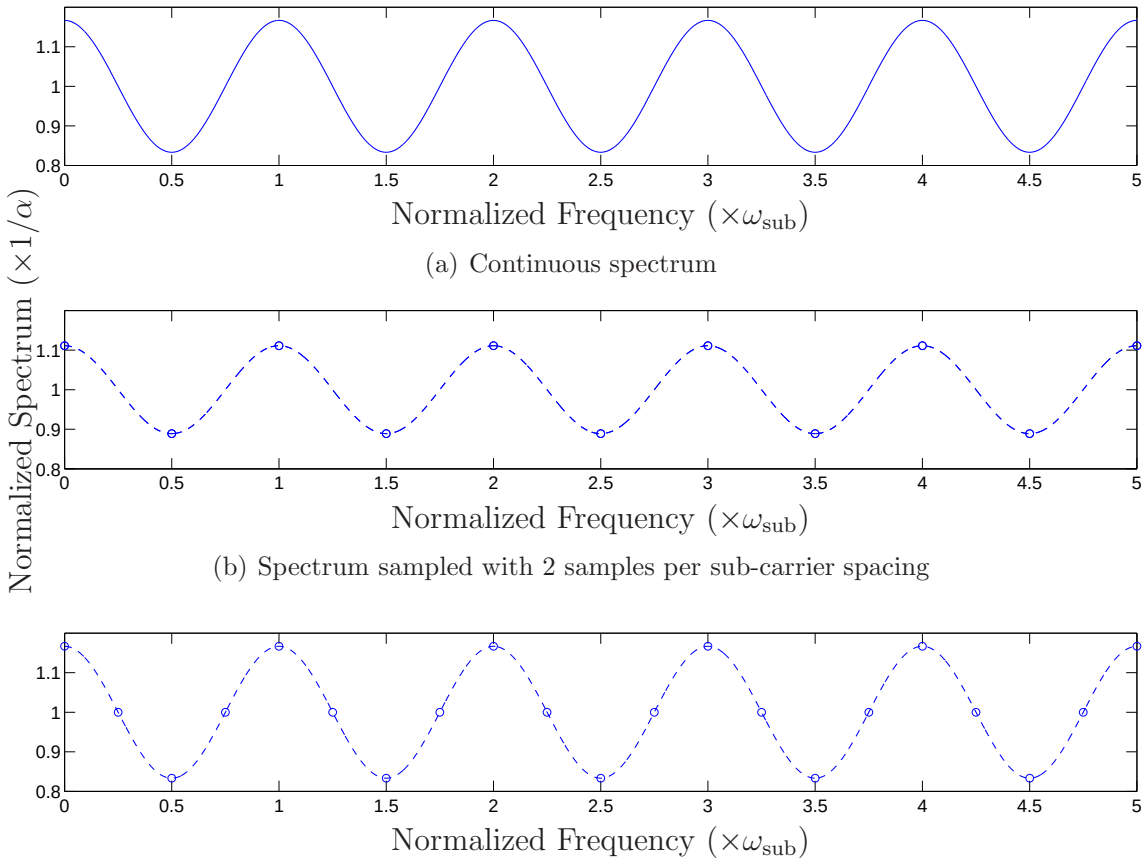

(a) Continuous spectrum

(b) Spectrum sampled with 2 samples per sub-carrier spacing

(c) Spectrum sampled with 4 samples per sub-carrier spacing

Figure 3.9: Illustration of power spectrum sampling

as the number of samples used in the computation increases. However, by averaging M such estimates, the variance will decrease as $1/M$. As such, the length of each individual data segment should be as small as possible to maximize the number of segments that can be averaged for a given number of received symbols.

When using a DFT to estimate the phase of a sinusoid, as will be done in Section 3.2.4, it is important that the number of samples per period be an integer. The Nyquist sampling theorem requires more than two samples per period. A rate of three or four samples per period will work fine. However, the FFT works on an interval which is a power of 2 samples. Therefore, the best choice is to use 4 samples in the FFT of Section 3.2.4. This means that the smallest segment length which can be used to estimate the power spectrum is $4N$, which will result in 4 samples per sub-carrier spacing.

The effects of averaging the magnitude square of several FFTs to obtain an estimate of the spectrum are illustrated in Figure 3.10. Figure 3.10 show three scenarios. In all three scenarios, the mean of the power spectrum estimator is the same. The variance of the estimator changes significantly however. Figure 3.10(a) and 3.10(b) illustrate that minimizing the spectral resolution of the estimate, and thereby maximizing the number of segments that can be averaged, greatly improves the performance of the estimator as described above. Once at the minimum practical spectral resolution, the number of symbols used to estimate the power spectrum becomes the primary control parameter with which to reduce the variance of the estimator. This is shown in Figure 3.10(c).

3.2.3 Information Band Isolator

Current standards like IEEE 802.16 specify a number of null carriers in the spectrum. As previously discussed in Chapter 2, these nulls are included at the band

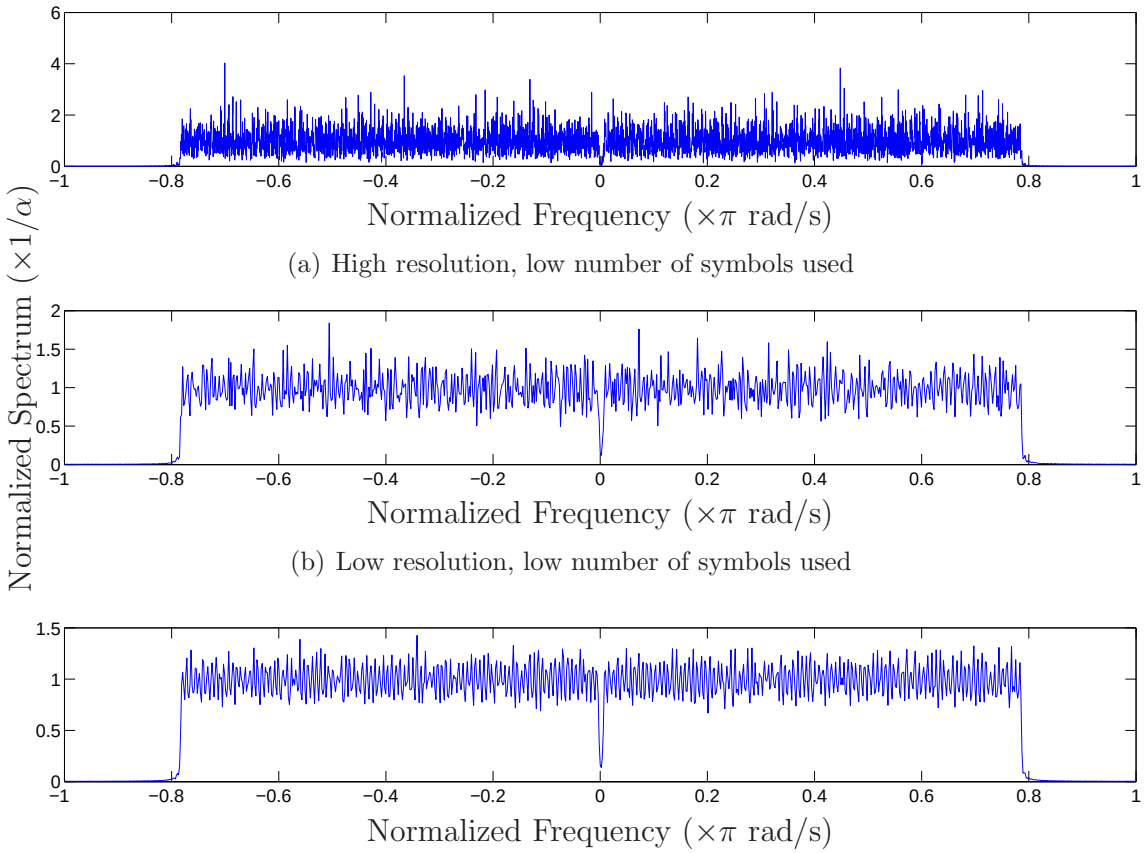

(a) High resolution, low number of symbols used

(b) Low resolution, low number of symbols used

(c) Low resolution, high number of symbols used

Figure 3.10: Averaging effects of the DFT length

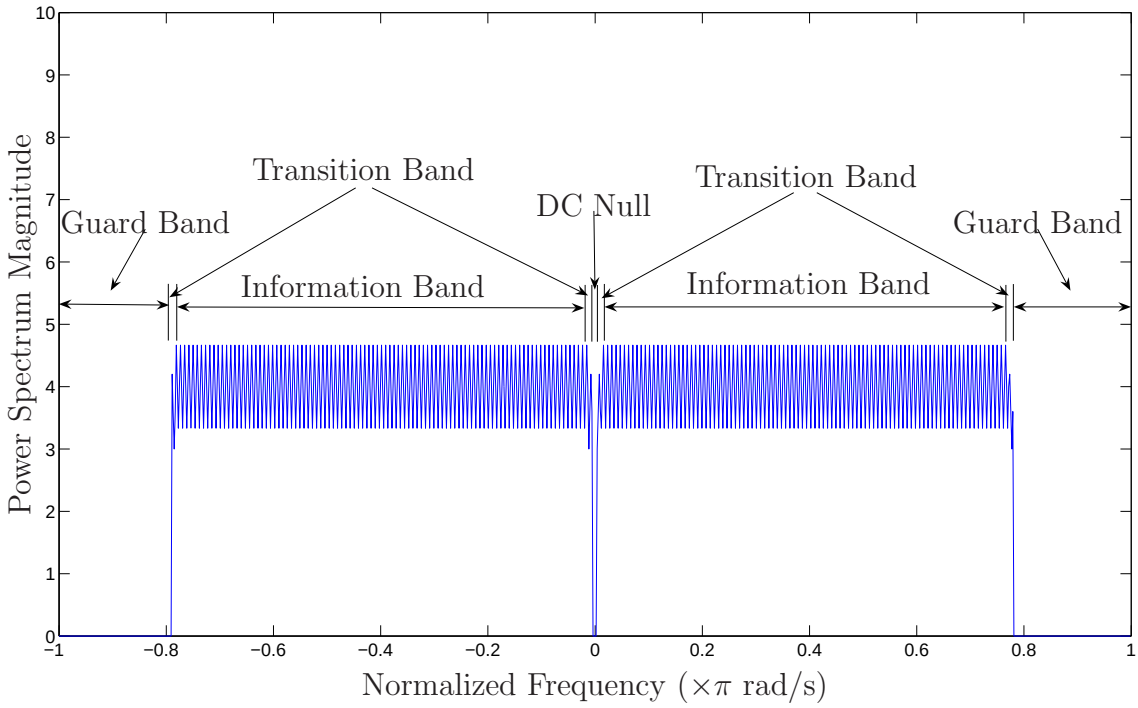

Figure 3.11: Power spectrum partitioning with transition bands shown

edges in order to limit out of band emissions. Similarly, the IEEE 802.16 standard specifies a DC null to help correct DC offsets introduced by zero-IF receivers.

As they contain no useful information, the samples of the power spectrum estimate in these null bands must be excluded. Practically, there is a transition between the information band and the guard band which is one sub-carrier wide. This means that one information bearing sub-carrier is removed at the edges of the information band. For the IEEE 802.16 standard, this means excluding 16 samples (4 sub-carrier spacings). Specifically, one spacing is excluded on either side of the DC null and one spacing at each guard band transition. The transition band is shown in Figure 3.11.

In order to isolate these samples, a coarse estimate of the integer part of the CFO is first necessary. As described in Section 2.4, these coarse estimators are well-

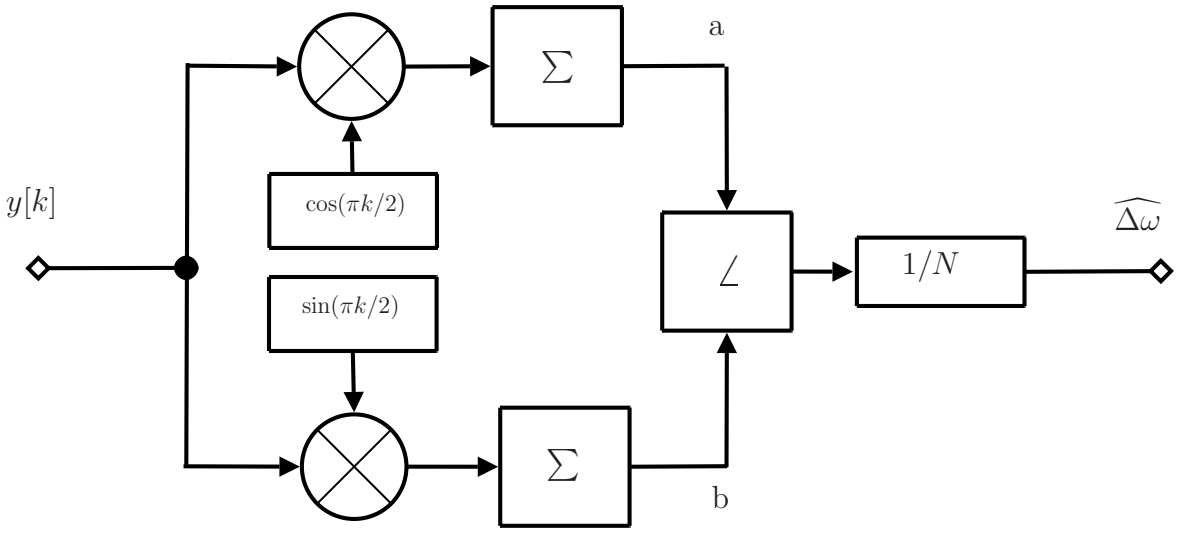

Figure 3.12: Diagram of CFO estimator block

established and relatively straightforward. Knowledge of the integer portion of the CFO can therefore be assumed to have been provided by an estimator like that presented in [25].

When isolating the useful portion of the power spectrum estimate, the resulting composite signal must have an integer number of full periods of the power spectrum's sinusoidal component. In order to facilitate this and to prevent phase discontinuities in the isolated signal, only integer multiples of α subsequent samples are removed.

3.2.4 Carrier Frequency Offset Estimator

Once the appropriate information bearing samples have been isolated, the resulting signal is a noisy estimate of a repeating raised sinusoid with a period equal to the sub-carrier spacing, and a phase shift proportional to the carrier frequency offset.

The carrier frequency offset estimator shown in Figure 3.12 calculates the Fourier

series coefficient of the isolated signal at the known frequency of the sinusoid.

$$a = \sum_{k=0}^{N_{\text{iso}}-1} y[k] \cos\left(\frac{2\pi}{\alpha}k\right) \tag{3.24}$$

$$b = \sum_{k=0}^{N_{\text{iso}}-1} y[k] \sin\left(\frac{2\pi}{\alpha}k\right) \tag{3.25}$$

where N_{iso} are the number of isolated information samples from the power spectrum estimate, $y[k]$. The sinusoid's phase shift and the corresponding frequency offset can then be estimated as:

$$\theta = \arctan\left(\frac{b}{a}\right) \tag{3.26}$$

$$\Delta\omega = \frac{\theta}{N} \tag{3.27}$$

where N is defined above as the number of samples in an OFDM signal, not including the cyclic prefix.

3.3 Variance Analysis

In order to characterize the proposed algorithm's theoretical performance, an expression for the variance of the estimator is derived. A model for the variance of the power spectral estimator is presented and used to approximate the final variance of the CFO estimate.

3.3.1 Variance Analysis of the Power Spectral Estimate

A complex low pass equivalent of an OFDM signal, as described in Sections 2.3 and 3.2, can be considered a stochastic process with a sample function represented by $x(n)$. This sample function is divided into segments $x_l(n)$ where an estimate of the power spectrum is obtained from the segmented sample function by

$$X_l(k)X_l^*(k) = \sum_{m=0}^{\alpha N-1} \sum_{n=0}^{\alpha N-1} x_l(n)x_l^*(m)e^{j\frac{2\pi k}{\alpha N}(n-m)} \tag{3.28}$$

where * denotes the complex conjugate and $x_l(n)$ are defined by $x(l\alpha N + n)$ for $n = 0, 1, \ldots \alpha N - 1$. Using one segment to estimate $X_l(k)X_l^*(k)$ as done in (3.28) will not produce a good estimate. As such, M estimates from different segments are averaged to obtain a better multiple-segment estimate of the power spectrum. The number of single segment estimates used in the multiple-segment estimator is given by

$$M = \frac{N_{\text{sym}}}{\alpha}\left(\frac{N + N_{CP}}{N}\right) \tag{3.29}$$

where N_{sym} is the number of symbols used in the CFO estimator.

$$X(k)X^*(k) = \frac{1}{M}\sum_{l=0}^{M-1} X_l(k)X_l^*(k) \tag{3.30}$$

$$X(k)X^*(k) = \frac{1}{M}\sum_{l=0}^{M-1}\sum_{m=0}^{\alpha N-1}\sum_{n=0}^{\alpha N-1} x_l(n)x_l^*(m)e^{j\frac{2\pi k}{\alpha N}(n-m)} \tag{3.31}$$

The variance of the multiple-segment estimator is denoted $\sigma_{\text{ps}}(k)^2$ and is given by

$$\sigma_{\text{ps}}(k)^2 = E\left[\left(X(k)X^*(k)\right)^2\right] - \mu(k)^2 \tag{3.32}$$

where $\mu(k) = E\left[X(k)X^*(k)\right]$ is the closed form expression for the mean given by (3.23). Using (3.31), the first term of (3.32) becomes

$$\begin{aligned} &E\left[\left(X(k)X^*(k)\right)^2\right] \\ &= E\left[\frac{1}{M^2}\sum_{l=0}^{M-1}\sum_{m=0}^{\alpha N-1}\sum_{n=0}^{\alpha N-1}\sum_{h=0}^{M-1}\sum_{s=0}^{\alpha N-1}\sum_{t=0}^{\alpha N-1} x_l(n)x_l^*(m)x_h(s)x_h^*(t)e^{j\frac{2\pi k}{\alpha N}(n-m+s-t)}\right] \end{aligned} \tag{3.33}$$

Equation (3.33) has 2 cases based upon the values of l and h. Each case will be addressed seperately.

$$E\left[\left(X(k)X^*(k)\right)^2\right] = G_1(k) + G_2(k) \tag{3.34}$$

where

$$G_1(k) = E\left[\left(X(k)X^*(k)\right)^2\right]; \quad h \neq l \tag{3.35}$$

and

$$G_2(k) = E\left[\left(X(k)X^*(k)\right)^2\right]; \quad h = l \tag{3.36}$$

In the first case of (3.34), the l^{th} and h^{th} estimates are taken from different segments of the received baseband OFDM signal. While not exactly true, if $x_l(n)x_l^*(m)$ and $x_h(s)x_h^*(t)$ are independent for different segments then $G_1(k)$ can be re-written as

$$\begin{aligned} G_1(k) = \; & \frac{1}{M^2} E\left[\sum_{l=0}^{M-1}\sum_{m=0}^{\alpha N-1}\sum_{n=0}^{\alpha N-1} x_l(n)x_l^*(m)e^{j\frac{2\pi k}{\alpha N}(n-m)}\right] \\ & \times E\left[\sum_{h=0,h\neq l}^{M-1}\sum_{s=0}^{\alpha N-1}\sum_{t=0}^{\alpha N-1} x_h(s)x_h^*(t)e^{j\frac{2\pi k}{\alpha N}(s-t)}\right] \end{aligned} \tag{3.37}$$

For most values of l and h, the l^{th} and h^{th} segments of the received baseband OFDM signal are not adjacent. As such, all of their samples come from different OFDM symbols with independent modulations. In the smaller number of cases where the h^{th} and l^{th} segments are adjacent, they share a rolling number of samples from the same OFDM symbol. Given the length of these segments, however, the majority of samples will be from different symbols with independent modulations. As such, 3.37 is a reasonable simplification. In this form, $G_1(k)$ is clearly not a function of l and h. As there are $M(M-1)$ cases where $h \neq l$, the double sum over l and h reduces to:

$$\begin{aligned} G_1(k) = \; & \frac{M(M-1)}{M^2} E\left[\sum_{m=0}^{\alpha N-1}\sum_{n=0}^{\alpha N-1} x_h(n)x_h^*(m)e^{j\frac{2\pi k}{\alpha N}(n-m)}\right] \\ & \times E\left[\sum_{s=0}^{\alpha N-1}\sum_{t=0}^{\alpha N-1} x_l(s)x_l^*(t)e^{j\frac{2\pi k}{\alpha N}(s-t)}\right] \end{aligned} \tag{3.38}$$

In (3.38), the two expectation operations are identical to the mean power spectrum, $\mu(k)$, which was calculated in Section 3.1. As such, (3.38) can be simplified to yield:

$$G_1(k) = \frac{M-1}{M}\mu^2(k) \tag{3.39}$$

In the second case of 3.34, there are M cases where $h = l$. In these instances, $G_2(k)$ is again clearly not a function of l. Since $e^{j\frac{2\pi k}{\alpha N}(n-m+s-t)}$ is not random, $G_2(k)$ can be expressed as

$$G_2(k) = \frac{1}{M} \sum_{m=0}^{\alpha N-1} \sum_{n=0}^{\alpha N-1} \sum_{s=0}^{\alpha N-1} \sum_{t=0}^{\alpha N-1} E\left[x_l(n)x_l^*(m)x_l(s)x_l^*(t)\right] e^{j\frac{2\pi k}{\alpha N}(n-m+s-t)} \tag{3.40}$$

The expectation in (3.40) can be easily evaluated using Isserlis' formula [28] if $x_l(n)$, $x_l^*(m)$, $x_l(s)$, and $x_l^*(t)$ are Gaussian random variables. The central limit theorem implies OFDM signals will be nearly Gaussian. Applying Isserlis' formula to the expectation in 3.40

$$\begin{aligned} E\left[x_l(n)x_l^*(m)x_l(s)x_l^*(t)\right] &= E\left[x_l(n)x_l^*(m)\right] E\left[x_l(s)x_l^*(t)\right] \\ &+ E\left[x_l(n)x_l(s)\right] E\left[x_l^*(m)x_l^*(t)\right] \\ &+ E\left[x_l(n)x_l^*(t)\right] E\left[x_l(s)x_l^*(m)\right] \end{aligned} \tag{3.41}$$

Inserting (3.41) into (3.40) produces:

$$\begin{aligned} &G_2(k) \\ &= \frac{1}{M} \sum_{n=0}^{\alpha N-1} \sum_{m=0}^{\alpha N-1} E\left[x_l(n)x_l^*(m)\right] e^{j\frac{2\pi k}{\alpha N}(n-m)} \sum_{s=0}^{\alpha N-1} \sum_{t=0}^{\alpha N-1} E\left[x_l(s)x_l^*(t)\right] e^{j\frac{2\pi k}{\alpha N}(s-t)} \\ &+ \frac{1}{M} \sum_{n=0}^{\alpha N-1} \sum_{s=0}^{\alpha N-1} E\left[x_l(n)x_l(s)\right] e^{j\frac{2\pi k}{\alpha N}(n+s)} \sum_{m=0}^{\alpha N-1} \sum_{t=0}^{\alpha N-1} E\left[x_l^*(m)x_l^*(t)\right] e^{-j\frac{2\pi k}{\alpha N}(m+t)} \\ &+ \frac{1}{M} \sum_{n=0}^{\alpha N-1} \sum_{t=0}^{\alpha N-1} E\left[x_l(n)x_l^*(t)\right] e^{j\frac{2\pi k}{\alpha N}(n-t)} \sum_{s=0}^{\alpha N-1} \sum_{m=0}^{\alpha N-1} E\left[x_l(s)x_l^*(m)\right] e^{j\frac{2\pi k}{\alpha N}(s-m)} \end{aligned} \tag{3.42}$$

Since

$$\mu(k) = \sum_{n=0}^{\alpha N-1} \sum_{m=0}^{\alpha N-1} E\left[x_l(n)x_l^*(m)\right] e^{j\frac{2\pi k}{\alpha N}(n-m)} \tag{3.43}$$

the top and bottom terms can be simplified such that (3.42) becomes

$$G_2(k) = \frac{2\mu^2(k)}{M} + \frac{1}{M}\sum_{n=0}^{\alpha N-1}\sum_{s=0}^{\alpha N-1} E\left[x_l(n)x_l(s)\right] e^{j\frac{2\pi k}{\alpha N}(n+s)} \sum_{m=0}^{\alpha N-1}\sum_{t=0}^{\alpha N-1} E\left[x_l^*(m)x_l^*(t)\right] e^{-j\frac{2\pi k}{\alpha N}(m+t)} \tag{3.44}$$

The middle term of (3.42) is difficult to analyze mathematically. However, numerical evaluation shows that it is approximately zero. Therefore, assuming that the contribution from the middle term in (3.42) is negligible, $G_2(k)$ reduces to,

$$G_2(k) \simeq \frac{2\mu^2(k)}{M}. \tag{3.45}$$

Substituting $G_1(k)$ from (3.39) and $G_2(k)$ from (3.45) into (3.34) and summing for the two cases yields,

$$\begin{aligned} E\left[\left(X(k)X^*(k)\right)^2\right] &= G_1(k) + G_2(k) \\ &= \frac{M-1}{M}\mu^2(k) + \frac{2}{M}\mu^2(k) \\ &= \left(1 + \frac{1}{M}\right)\mu^2(k) \end{aligned} \tag{3.46}$$

Evaluating the variance expression in (3.32) with (3.46) produces a final expression for the theoretical variance of the power spectrum estimator. This variance is given by:

$$\begin{aligned} \sigma_{\text{ps}}(k)^2 &= \left(1 + \frac{1}{M}\right)\mu^2(k) - \mu(k)^2 \\ \sigma_{\text{ps}}(k)^2 &= \frac{1}{M}\mu^2(k). \end{aligned} \tag{3.47}$$

3.3.2 Variance Analysis of the Carrier Frequency Offset Estimator

Equation (3.23) on page 29 illustrates that the power spectrum of the received signal is a raised sinusoid with a period equal to the frequency spacing between subcarriers. It also illustrates that an offset in the carrier frequency causes a phase shift

in the sinusoid. Given an additive white Gaussian noise (AWGN) channel and a finite number of symbols used in the estimator, the estimate of the power spectrum is corrupted with noise, which will be denoted $q(k)$. This noise has two components. One is caused by the additive white Gaussian (AWG) channel noise, and the other is caused by the signal itself. The latter is often referred to as pattern dependent noise or self-noise. Assuming that both noise components are independent Gaussian random variables, their sum is also Gaussian with a variance equal to the sum of the component variances. Therefore, the variance of the sum, i.e. the variance of $q(k)$, denoted $\sigma_q^2(k)$ can be expressed as:

$$\sigma_q^2(k) = \sigma_{ps}^2(k) + \sigma_n^2 \tag{3.48}$$

$$= \frac{1}{M}\mu^2(k) + \frac{1}{M}\sigma_n^2 \tag{3.49}$$

Recall $\mu(k)$ is the mean power spectrum defined in equation (3.23) on page 29 to be

$$\mu(k) = \alpha + 2(\alpha - 1)\frac{N_{CP}}{N + N_{CP}} \cos(\frac{2\pi}{\alpha}k + \Delta\omega N). \tag{3.50}$$

In the proposed algorithm, the phase angle of the sinusoidal component of the power spectrum is estimated using a Fourier series and an inverse tangent function. Although computationally more complex, another valid method for estimating the phase would be to use a fine-meshed global search. It can be shown, as is presented in [29] [30], that both estimators converge to the same value and are equivalent. This equivalence is utilized in the variance analysis. The variance analysis of the Fourier method of angle estimation is quite protracted, while the variance analysis of the fine-meshed global search is straight forward. Therefore, the variance of the Fourier series based estimate is obtained by analyzing the fine-meshed global search estimator.

The estimated power spectrum is a sample sequence, N_{iso} of which are information

bearing. The information bearing samples can be expressed as,

$$\hat{S}_{xx}(k) = \alpha + 2(\alpha - 1)\frac{N_{CP}}{N + N_{CP}} \cos(\frac{2\pi}{\alpha}k + \Delta\omega N) + q(k). \tag{3.51}$$

It may appear strange that $\hat{S}_{xx}(k)$ is a pure single-frequency sinusoid corrupted with noise when it is a concatenation of information bearing segments of the spectrum. The reason for this is that the segments removed from the spectrum have a length that are an integer multiple of the sinusoid's period, α. Therefore, taking out the guard and transmission band samples and concatenating the information bands does not introduce a phase discontinuity in the sinusoid.

To simplify notation, the constant $2(\alpha - 1)\frac{N_{CP}}{N+N_{CP}}$ is denoted β, the frequency $2\pi/\alpha$ is denoted ω_o, and the phase shift $\Delta\omega N$ is denoted ϕ. With this simplified notation, (3.51) reduces to

$$\hat{S}_{xx}(k) = \alpha + \beta \cos(\omega_o k + \phi) + q(k) \tag{3.52}$$

To estimate ϕ, the fine-meshed global search maximizes a correlation with sinusoid $cos(\omega_o k + \theta)$ with respect to θ. As this function is a measure of the power in the sinusoidal component of $\hat{S}_{xx}(k)$, it is denoted $P(\theta)$ and is given by:

$$P(\theta) = \sum_{k=0}^{N_{\text{iso}}-1} (\alpha + \beta \cos(\omega_o k + \phi))\, cos(\omega_o k + \theta) + \sum_{k=0}^{N_{\text{iso}}-1} q[k] \cos(\omega_o k \theta) \tag{3.53}$$

The value of θ that maximizes $P(\theta)$ is used to estimate ϕ, i.e. $\hat{\phi} = \theta : P(\theta)$ is maximum.

Equation (3.53) has two components. The first component is the noise-free term, which will be denoted $P_{\text{NF}}(\theta)$, and the second component is the noise term, which will be denoted $P_{\text{N}}(\theta)$.

$$P(\theta) = P_{\text{NF}}(\theta) + P_{\text{N}}(\theta) \tag{3.54}$$

where

$$P_{\mathrm{NF}}(\theta) = \sum_{k=0}^{N_{\mathrm{iso}}-1} (\alpha + \beta\cos(\omega_o k + \phi))\cos(\omega_o k + \theta) \tag{3.55}$$

and

$$P_{\mathrm{N}}(\theta) = \sum_{k=0}^{N_{\mathrm{iso}}-1} q(k)\cos(\omega_o k + \theta). \tag{3.56}$$

Each component can be approximated by a second order Taylor series expansion about $\theta = \phi$. This approach is a variation of the one used in [31].

For the first term, the second order Taylor series taken about $\theta = \phi$ is

$$P_{\mathrm{NF}}(\theta) = P_{\mathrm{NF}}(\phi) + \left.\frac{dP_{\mathrm{NF}}(\theta)}{d\theta}\right|_{\theta=\phi}(\phi - \theta) + \left.\frac{d^2P_{\mathrm{NF}}(\theta)}{d\theta^2}\right|_{\theta=\phi}\frac{(\phi-\theta)^2}{2}. \tag{3.57}$$

The first derivative $\frac{dP_{\mathrm{NF}}(\theta)}{d\theta}$ is zero at the maximum point $\theta = \phi$. Taking the second derivative of $P(\theta)$ with respect to θ and evaluating (3.57) yields,

$$P_{\mathrm{NF}}(\theta) = \sum_{k=0}^{N_{\mathrm{iso}}-1} (\alpha + \beta\cos(\omega_o k + \phi))\,cos(\omega_o k + \phi) + \sum_{k=0}^{N_{\mathrm{iso}}-1} \beta\cos^2(\omega_o k + \phi)\frac{(\phi-\theta)^2}{2}. \tag{3.58}$$

For notational convenience, we can express $(\phi - \theta) = \Delta\theta$, which serves as a reminder that $\Delta\theta$ is small. Making this substitution produces,

$$P_{\mathrm{NF}}(\phi + \Delta\theta) = \sum_{k=0}^{N_{\mathrm{iso}}-1} (\alpha + \beta\cos(\omega_o k + \phi))\,cos(\omega_o k + \phi) + \sum_{k=0}^{N_{\mathrm{iso}}-1} \beta\cos^2(\omega_o k + \phi)\frac{\Delta\theta^2}{2}. \tag{3.59}$$

For the noise term, the second order Taylor series taken about $\theta = \phi$ is given by

$$\begin{aligned} P_{\mathrm{N}}(\theta) &= P_{\mathrm{N}}(\phi) + \left.\frac{dP_{\mathrm{N}}(\theta)}{d\theta}\right|_{\theta=\phi}(\phi - \theta) + \left.\frac{d^2P_{\mathrm{N}}(\theta)}{d\theta^2}\right|_{\theta=\phi}\frac{(\phi-\theta)^2}{2} \\ &= \sum_{k=0}^{N_{\mathrm{iso}}-1} q(k)\cos(\omega_o k + \phi) - \sum_{k=0}^{N_{\mathrm{iso}}-1} q(k)\sin(\omega_o k + \phi)(\phi - \theta) \\ &\quad - \sum_{k=0}^{N_{\mathrm{iso}}-1} q(k)\cos(\omega_o k + \phi)\frac{(\phi-\theta)^2}{2} \end{aligned} \tag{3.60}$$

Converting to the Taylor series as a function of $\Delta\theta$, (3.61) becomes

$$P_{\mathrm{N}}(\phi+\Delta\theta) = \sum_{k=0}^{N_{\mathrm{iso}}-1} q(k)\cos(\omega_o k+\phi) - \sum_{k=0}^{N_{\mathrm{iso}}-1} q(k)\sin(\omega_o k+\phi)\Delta\theta - \sum_{k=0}^{N_{\mathrm{iso}}-1} q(k)\cos(\omega_o k+\phi)\frac{\Delta\theta^2}{2} \tag{3.61}$$

For a fine mesh global search with small $\Delta\theta$, the first order term $\Delta\theta$ will dominate the second order $\Delta\theta^2/2$. Given that the summation terms have roughly the same magnitude, the second order term can be ignored such that

$$P_{\mathrm{N}}(\phi+\Delta\theta) = \sum_{k=0}^{N_{\mathrm{iso}}-1} q(k)\cos(\omega_o k+\phi) - \sum_{k=0}^{N_{\mathrm{iso}}-1} q(k)\sin(\omega_o k+\phi)\Delta\theta \tag{3.62}$$

The maximum of the combined expression $P(\phi+\Delta\theta) = P_{\mathrm{NF}}(\phi+\Delta\theta)+P_{\mathrm{N}}(\phi+\Delta\theta)$ is obtained by setting $\frac{dP(\phi+\Delta\theta)}{d\Delta\theta} = 0$ and solving for $\Delta\theta$. This begins with the expression for $P(\phi+\Delta\theta)$:

$$P(\phi+\Delta\theta) = \sum_{k=0}^{N_{\mathrm{iso}}-1} (\alpha+\beta\cos(\omega_o k+\phi))\,cos(\omega_o k+\phi) + \sum_{k=0}^{N_{\mathrm{iso}}-1} \beta\cos^2(\omega_o k+\phi)\frac{\Delta\theta^2}{2} + \sum_{k=0}^{N_{\mathrm{iso}}-1} q(k)\cos(\omega_o k+\phi) - \sum_{k=0}^{N_{\mathrm{iso}}-1} q(k)\sin(\omega_o k+\phi)\Delta\theta \tag{3.63}$$

Taking the derivative with respect to $\Delta\theta$ yields

$$\frac{dP(\phi+\Delta\theta)}{d\Delta\theta} = 0 + \sum_{k=0}^{N_{\mathrm{iso}}-1} \beta\cos^2(\omega_o k+\phi)\Delta\theta + 0 - \sum_{k=0}^{N_{\mathrm{iso}}-1} q(k)\sin(\omega_o k+\phi) \tag{3.64}$$

Setting $\frac{dP(\phi+\Delta\theta)}{d\Delta\theta} = 0$ and re-arranging yields

$$\Delta\theta = \frac{\sum_{k=0}^{N_{\mathrm{iso}}-1} q(k)\sin(\omega_o k+\phi)}{\sum_{k=0}^{N_{\mathrm{iso}}-1} \beta\cos^2(\omega_o k+\phi)} \tag{3.65}$$

Given that there are an integer number of periods of the sinusoid in the N_{iso} information bearing samples, the bottom term of (3.65) is a constant such that,

$$\Delta\theta = \frac{\sum_{k=0}^{N_{\mathrm{iso}}-1} q(k)\sin(\omega_o k+\phi)}{\frac{N_{\mathrm{iso}}}{2}\beta} \tag{3.66}$$

The variance of the fine-meshed global search estimator of phase shift is given by

$$\sigma^2_{\Delta\theta} = E[\Delta\theta^2] - E[\Delta\theta]^2. \tag{3.67}$$

The expected value of $\Delta\theta$ is obtained using (3.66). After moving the expectation operator inside the sum it becomes,

$$E[\Delta\theta] = \frac{\sum_{k=0}^{N_{\text{iso}}-1} E[q(k)] \sin(\omega_o k + \phi)}{\frac{N_{\text{iso}}}{2}\beta} \tag{3.68}$$

Given that $E[q(k)] = 0$, the expected value of $\Delta\theta$ is also zero.

The $E[\Delta\theta^2]$ is also evaluated using (3.66). The square of (3.66) is written as a double sum.

$$E[\Delta\theta^2] = \frac{\sum_{k=0}^{N_{\text{iso}}-1} \sum_{m=0}^{N_{\text{iso}}-1} E[q(k)q(m)] \sin(\omega_o k + \phi) \sin(\omega_o m + \phi)}{\left(\frac{N_{\text{iso}}}{2}\beta\right)^2} \tag{3.69}$$

When $m \neq k$, $q(k)$ and $q(m)$ are independent and the expected value of their product is zero. As such, the double sum can be reduced to a single summation over k as,

$$E[\Delta\theta^2] = \frac{\sum_{k=0}^{N_{\text{iso}}-1} E[q^2(k)] \sin^2(\omega_o k + \phi)}{\left(\frac{N_{\text{iso}}}{2}\beta\right)^2} \tag{3.70}$$

With $E[q(k)] = 0$, $E[q(k)^2]$ is the variance given by (3.48). Substituting (3.48) into (3.70) produces,

$$E[\Delta\theta^2] = \frac{\sum_{k=0}^{N_{\text{iso}}-1} \mu^2(k) \sin^2(\omega_o k + \phi)}{M\left(\frac{N_{\text{iso}}}{2}\beta\right)^2} + \frac{\sum_{k=0}^{N_{\text{iso}}-1} \sigma_n^2 \sin^2(\omega_o k + \phi)}{M\left(\frac{N_{\text{iso}}}{2}\beta\right)^2} \tag{3.71}$$

Expanding $\mu^2(k)$ and simplifying yields,

$$\begin{aligned}
E[\Delta\theta^2] &= \frac{\sum_{k=0}^{N_{\text{iso}}-1}\left(\alpha+\beta\cos(\omega_o k+\phi)\right)^2\sin^2(\omega_o k+\phi)}{M\left(\frac{N_{\text{iso}}}{2}\beta\right)^2} + \frac{\sum_{k=0}^{N_{\text{iso}}-1}\sigma_n^2\sin^2(\omega_o k+\phi)}{M\left(\frac{N_{\text{iso}}}{2}\beta\right)^2} \\
&= \frac{\sum_{k=0}^{N_{\text{iso}}-1}\alpha^2\sin^2(\omega_o k+\phi)}{M\left(\frac{N_{\text{iso}}}{2}\beta\right)^2} + \frac{\sum_{k=0}^{N_{\text{iso}}-1}\alpha\beta\cos(\omega_o k+\phi)\sin^2(\omega_o k+\phi)}{M\left(\frac{N_{\text{iso}}}{2}\beta\right)^2} \\
&+ \frac{\sum_{k=0}^{N_{\text{iso}}-1}\beta^2\cos^2(\omega_o k+\phi)\sin^2(\omega_o k+\phi)}{M\left(\frac{N_{\text{iso}}}{2}\beta\right)^2} + \frac{\sum_{k=0}^{N_{\text{iso}}-1}\sigma_n^2\sin^2(\omega_o k+\phi)}{M\left(\frac{N_{\text{iso}}}{2}\beta\right)^2} \\
&= \frac{\frac{N_{\text{iso}}}{2}\alpha^2}{M\left(\frac{N_{\text{iso}}}{2}\beta\right)^2} + 0 + \frac{\sum_{k=0}^{N_{\text{iso}}-1}\beta^2\cos^2(\omega_o k+\phi)\sin^2(\omega_o k+\phi)}{M\left(\frac{N_{\text{iso}}}{2}\beta\right)^2} + \frac{\frac{N_{\text{iso}}}{2}\sigma_n^2}{M\left(\frac{N_{\text{iso}}}{2}\beta\right)^2} \\
E[\Delta\theta^2] &= \frac{2\alpha^2}{MN_{\text{iso}}\beta^2} + \frac{\sum_{k=0}^{N_{\text{iso}}-1}\cos^2(\omega_o k+\phi)\sin^2(\omega_o k+\phi)}{M\left(\frac{N_{\text{iso}}}{2}\right)^2} + \frac{2\sigma_n^2}{MN_{\text{iso}}\beta^2} \qquad (3.72)
\end{aligned}$$

The middle term of (3.72) is a small bias, which will be denoted $\gamma(\phi)$. When there is no CFO, $\gamma(\phi)$ is zero. When the CFO is at its maximum value of $\pm 1/2$ of the sub-carrier spacing, the bias is a factor of more than 200 smaller than the sum of the other terms.

$$E[\Delta\theta^2] = \frac{2\alpha^2}{MN_{\text{iso}}\beta^2} + \gamma(\phi) + \frac{2\sigma_n^2}{MN_{\text{iso}}\beta^2} \qquad (3.73)$$

The constants $\beta = 2(\alpha-1)\frac{N_{CP}}{N+N_{CP}}$ and $M = \frac{N_{\text{sym}}}{\alpha}\left(\frac{N+N_{CP}}{N}\right)$ were used above to simplify notation. However, the final expression for the variance of the CFO estimator should be in terms of the variable system parameters (specifically the cyclic prefix length and the number of symbols used in the estimator). Since $E[\Delta\theta] = 0$, expanding these constants and substituting into (3.67)produces,

$$\sigma^2_{\Delta\theta} = \frac{\alpha^3 N(N+N_{\text{CP}})}{2(\alpha-1)^2 N_{\text{iso}}N_{\text{sym}}N_{\text{CP}}^2} + \frac{\alpha N(N+N_{\text{CP}})\sigma_n^2}{2(\alpha-1)^2 N_{\text{iso}}N_{\text{sym}}N_{\text{CP}}^2} + \gamma(\phi) \qquad (3.74)$$

Recall that the phase shift of the sinusoidal component of the power spectrum is related to the CFO as $\phi = \Delta\omega N$. As such, $\sigma^2_{\text{CFO}} = \sigma^2_{\Delta\theta}/N^2$.

$$\sigma^2_{\text{CFO}} = \frac{\alpha^3(N+N_{\text{CP}})}{2N(\alpha-1)^2 N_{\text{iso}}N_{\text{sym}}N_{\text{CP}}^2} + \frac{\alpha(N+N_{\text{CP}})\sigma_n^2}{2N(\alpha-1)^2 N_{\text{iso}}N_{\text{sym}}N_{\text{CP}}^2} + \frac{\gamma(\phi)}{N^2} \qquad (3.75)$$

In the literature, the standard convention is to display the CFO normalized to the sub-carrier spacing, $\omega_{\text{sub}} = \frac{2\pi}{N}$. For display purposes, the normalized CFO variance shown is therefore divided by ω_{sub}^2 and is given by:

$$\sigma^2_{\text{CFO}_{\text{norm}}} = \frac{\alpha^3 N(N+N_{\text{CP}})}{8\pi^2(\alpha-1)^2 N_{\text{iso}} N_{\text{sym}} N_{\text{CP}}^2} + \frac{\alpha N(N+N_{\text{CP}})\sigma_n^2}{8\pi^2(\alpha-1)^2 N_{\text{iso}} N_{\text{sym}} N_{\text{CP}}^2} + \frac{\gamma(\phi)}{4\pi^2} \tag{3.76}$$

4. ANALYSIS VERIFICATION VIA SIMULATION

Chapter 3 proposed and analyzed a blind carrier frequency offset algorithm. This chapter verifies the mathematics of this analysis via simulation.

The algorithm's power spectrum estimator, as described in Section 3.2.2, is simulated. The mean and the variance of the estimator's output are compared to their mathematically predicted values. The pattern dependent noise (also known as self-noise) of the power spectrum estimator is shown to be Gaussian, which confirms a critical assumption made in Section 3.3.2.

A series of simulations are then conducted by individually varying each of the system parameters in the algorithm. This illustrates how the variance of the carrier frequency offset estimator is effected by these various parameters. These simulated effects are compared to those predicted by the mathematically derived variance expression.

4.1 Simulation Setup

4.1.1 OFDM Signal Characteristics

Simulations of the proposed algorithm use an 256-OFDM signal similar to that specified in the IEEE 802.16 standard [20].

In the IEEE 802.16 standard an OFDM symbol consists of data, pilot, and null sub-carriers. While explained earlier, it is worth briefly repeating the functions data,

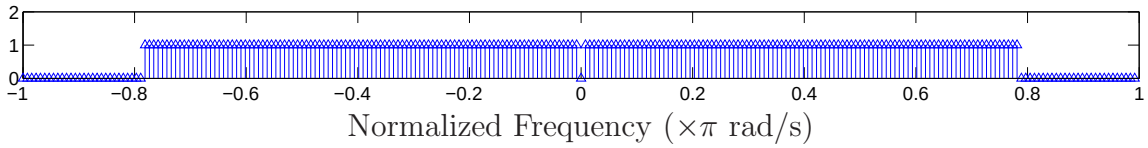

Figure 4.1: OFDM symbol spectral arrangement

pilot, and null sub-carriers. Pilot sub-carriers have various functions within a receiver. For example, they can be used to equalize the channel. They can also be used to facilitate frequency recovery. Null sub-carriers serve two purposes in the standard. First, a null at DC is included to allow for the correction of DC offsets introduced by local oscillator feed through in the zero-IF downconversion process. Second, nulls at the band edges create a guard band. This is necessary for practical filters to help limit out of band emissions. Inclusion of null tones limits the capacity of the system as it takes away data carrying sub-carriers. As such, the null tones are included as specified.

For the purposes of these simulations, each OFDM symbol is created from a mix of null and data sub-carriers using a 256 point IFFT. The spectral arrangement of this symbol is shown in Figure 4.1.

A cyclic prefix, as described in Chapter 2, is inserted at the start of each OFDM symbol. The IEEE 802.16a standard specifies the length of the cyclic prefix to be one of three possible values determined by the current channel conditions. The possible lengths are 1/4, 1/8, and 1/16 of the symbol period, which correspond to 16 samples, 32 samples, and 64 samples, respectively, for an IFFT length of 256 samples.

4.1.2 Channel Characteristics

In this chapter a flat AWGN channel is used. A more practical multipath channel is used in Chapter 5.

Table 4.1: Simulation Reference Parameters

Parameter Name	**Reference Value(s)**
Number of Repeated Trials	10000
Transmitted center frequency	5 GHz
Signal bandwidth	20 MHz
IFFT length, N (samples)	256
Number of sub-carriers transmitted	200
Number of information sub-carriers, N_{iso}	196
Frequency indices of guard sub-carriers	[-128..-101 101..127]
Frequency indices of data sub-carriers	[-100..-1 1..100]
Modulation Type*	QPSK
Cyclic Prefix Length*, N_{cp} (samples)	32
Carrier Frequency Offset*, $\Delta\omega$ (normalized to one sub-carrier spacing)	0.2
Number of Symbols Reveived*	100
Estimator Segment Length, αN (samples)	1024

*Parameters marked with an asterisk are varied one at a time in Section 4.3

4.1.3 Simulation Parameters

The MATLAB file used to simulate the proposed algorithm is presented in Appendix A. A set of base reference parameters for the simulations is presented in Table 4.1. These parameters are used in simulations throughout the chapter. Though one trial executes very quickly, MATLAB processes for loops quite slowly. As such, each data point with 10000 repeated trials of 100 symbols each requires approximately 5-10 minutes to generate.

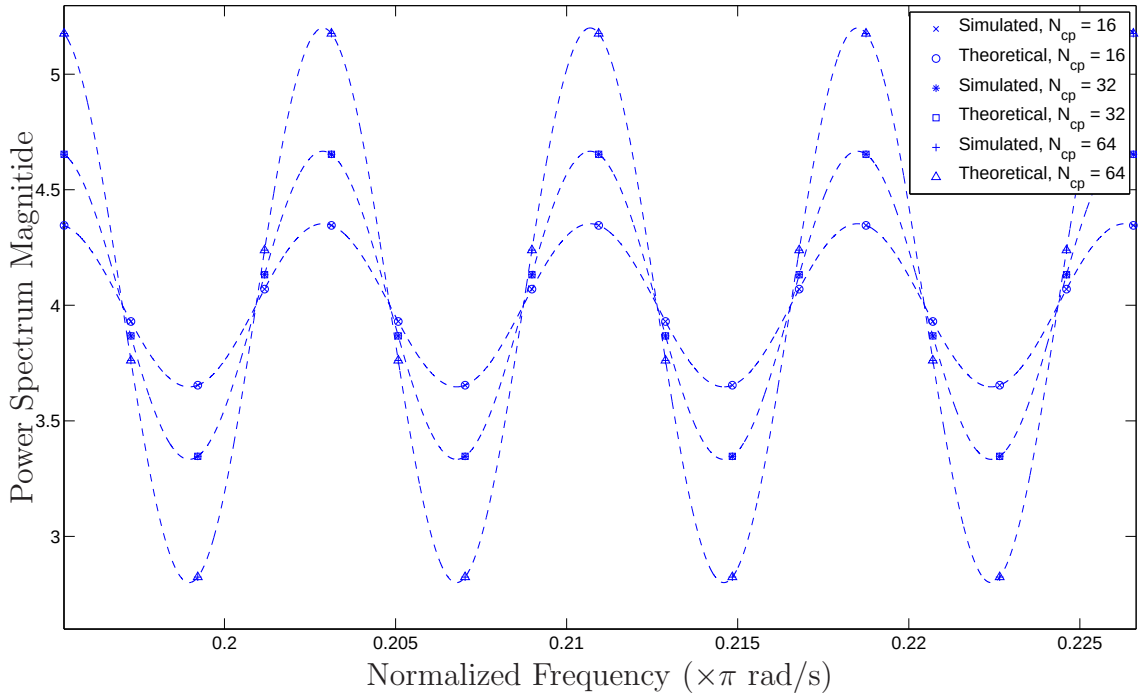

Figure 4.2: Comparison of simulated and theoretical power spectrum means in the information band

4.2 Verification of Power Spectrum Estimator Characteristics

4.2.1 Power Spectrum Estimator Mean

The received signal's theoretical power spectrum was calculated to be a raised cosine in Section 3.1. Using the above MATLAB simulation, the multi-segment power spectrum estimates from repeated trials are averaged together. Figure 4.2 shows a zoomed in view of the mean multi-segment estimator for all three cyclic prefix lengths. It compares these averages to the theoretical expected value given by Equation (3.23) on page 29. It should be noted that neither x or y axes start at the origin.

For all three cyclic prefix lengths, the simulated mean power spectrum closely

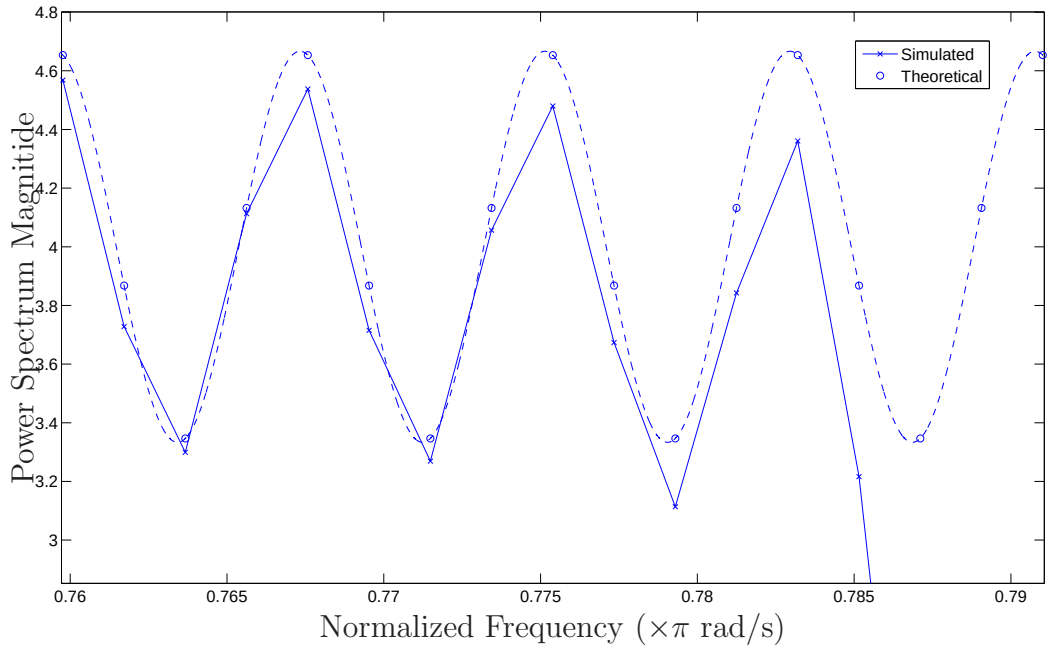

Figure 4.3: Comparison of simulated and theoretical power spectrum means in the transition band

matches the mathematically calculated spectrum in the region shown in Figure 4.2. This remains true across the power spectrum's entire information band.

Section 3.2.3 describes a transition band between the information bearing sub-carriers and the null sub-carriers. Figure 4.3 shows a zoomed in section of the simulated estimator mean in the transition region. The transition band in Figure 4.3 clearly requires more than one period of the power spectrum's sinusoidal component before it exactly matches the theoretical mean. However, when considering the noise on the power spectrum estimates, the difference is minor beyond the first sub-carrier spacing of this band. While these non-ideal samples will introduce some additional noise into the estimator, they remain beneficial to include in the estimator for they do contribute more signal than noise.

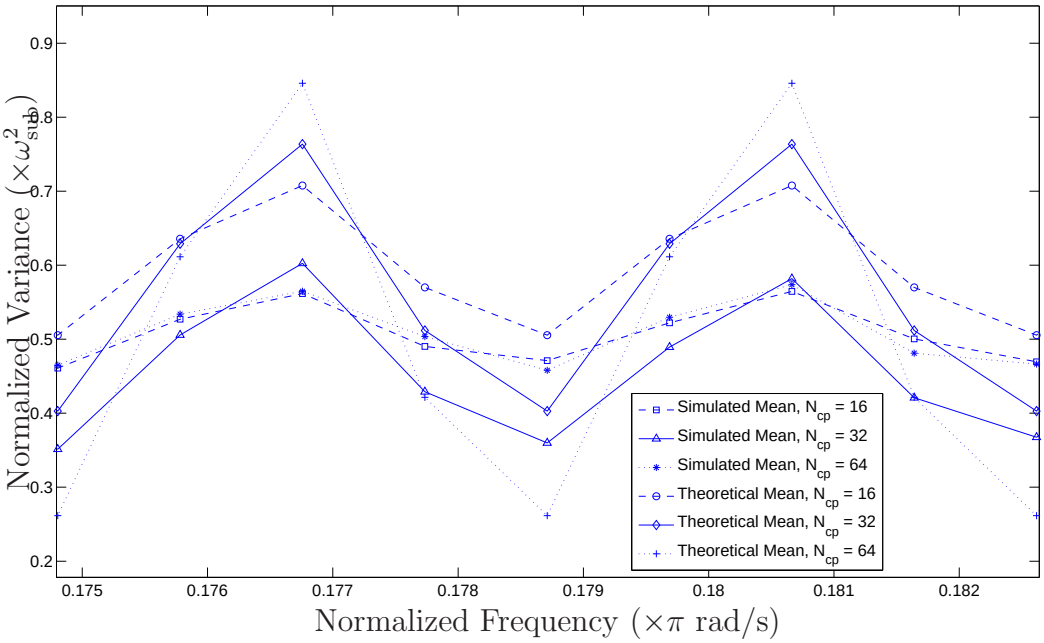

Figure 4.4: Comparison of Simulated and Theoretical Power Spectrum Estimator Variance

4.2.2 Power Spectrum Estimator Variance

A finite number of symbols are used to estimate the received signal's power spectrum. As such, the estimate will be corrupted with pattern-dependent noise. In order to verify the mathematically calculated variance of this noise, the proposed estimator is simulated for a number of repeated trials with no AWG channel noise. Figure 4.4 compares the simulated variance with the variance derived in Section 3.3.1 for the power spectrum estimator's pattern-dependent noise. Once again, note that the axes do not begin at the origin as this is a zoomed in section of the spectrum.

Figure 4.4 shows that some discrepancy between the theoretical and simulated results is introduced by the assumptions made in the mathematical analysis. This is mitigated somewhat by the averaging across the spectrum. This averaging is done

when the proposed algorithm estimates the phase shift of the spectrum's sinusoidal component. When the average variance is examined, the simulated average is close to the mathematically predicted values. As such, the predicted power spectrum variance is verified to be a reasonable approximation.

4.2.3 Power Spectrum Estimator Pattern-Dependent Noise Distribution

When deriving an equation for the variance of the CFO estimate, the assumption was made that the pattern-dependent noise of the power spectrum estimator was Gaussian. Figure 4.5 presents the distribution of the simulated results for one point in the power spectrum and compares it to a theoretical Gaussian distribution with the same mean and variance. This process was repeated for different samples of the spectrum. In all cases, the distribution appeared to be nearly Gaussian, thereby verifying this important assumption.

4.3 System Parameter Effects on CFO Estimator Variance

The mathematics in Section 3.3.2 predict that the variance of the CFO estimator will be determined by the length of the OFDM cyclic prefix, the number of symbols used in the estimator, and the channel SNR. A series of simulations are performed where each of these parameters is individually varied. The simulation results are compared to the theoretical results. The effects of changing other system parameters are also checked even though the theory predicts these parameters will not impact performance.

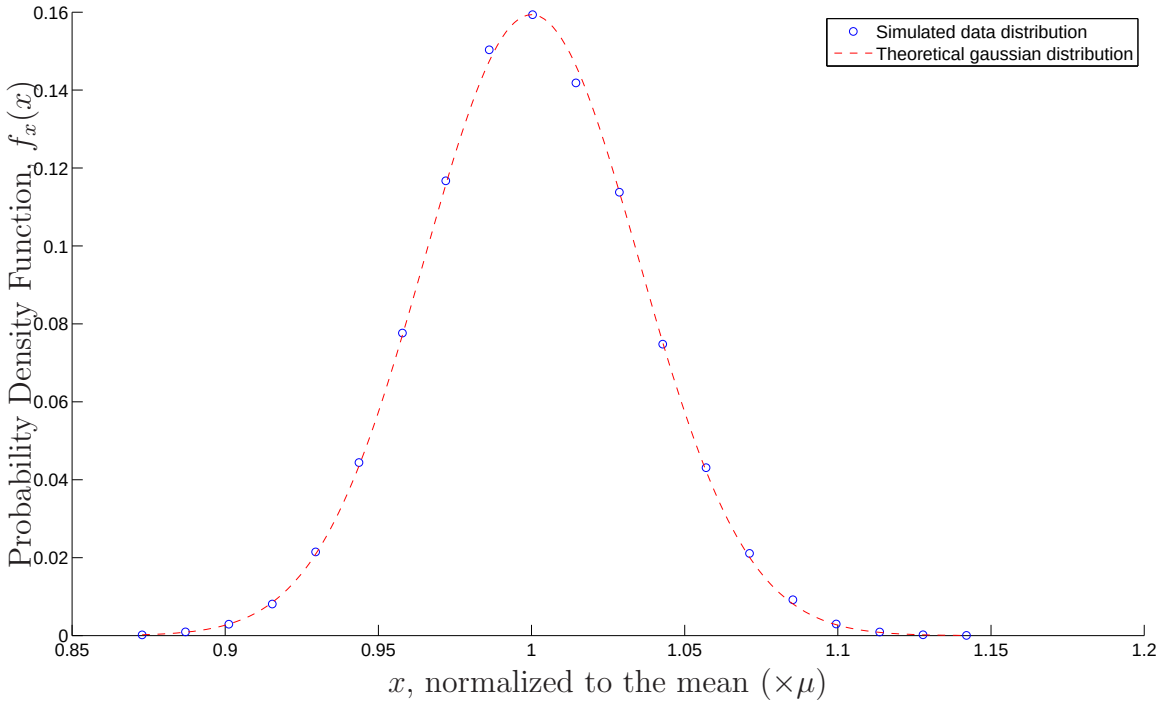

Figure 4.5: PDF of one output point from the power spectrum estimator

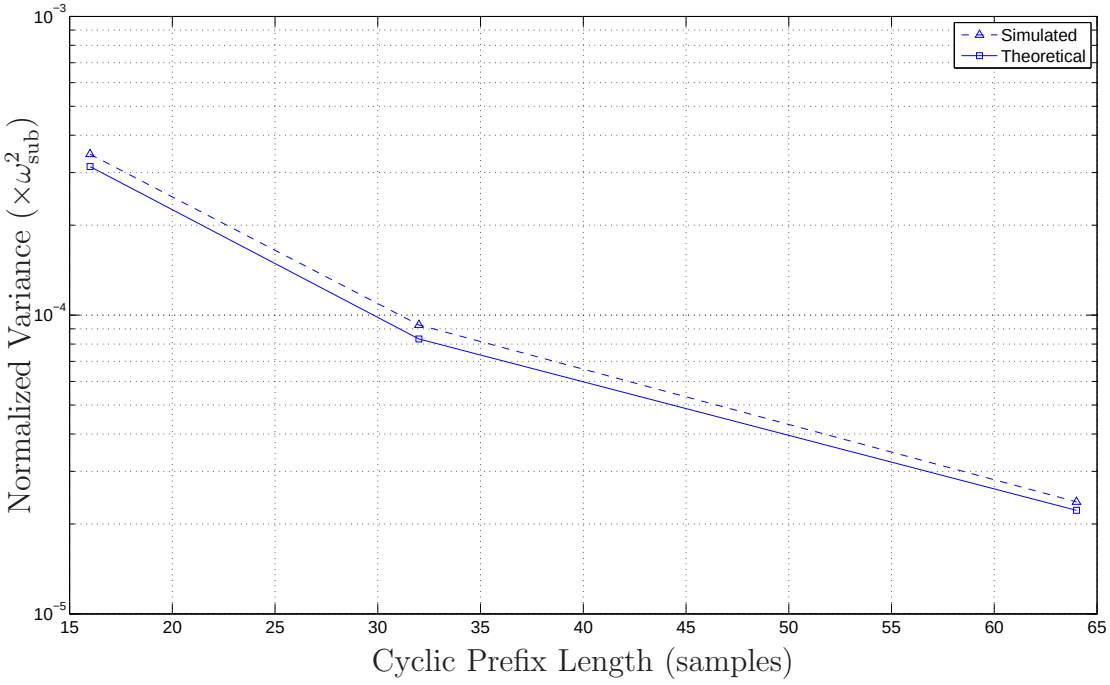

Figure 4.6: Effect of varying the cyclic prefix length for a symbol of 256 samples

4.3.1 Effects of the Cyclic Prefix Length

The length of the cyclic prefix is restricted to one of three possible values determined by the current channel conditions. As such, it cannot be used as a control parameter for adjusting the algorithm's performance. That said, the mathematics in Chapter 3 predict that the length of the cyclic prefix will have a significant impact on the variance of the CFO estimator that must be characterized.

While holding all other parameters constant as listed in Table 4.1, the cyclic prefix length is varied between 16, 32, and 64 samples. Theoretically, from Equation (3.76) on page 50, the length of the cyclic prefix, N_{CP}, scales the estimator variance as $\frac{N+N_{\text{CP}}}{N_{\text{CP}}^2}$. Figure 4.6 compares this theory with the simulations.

The simulated variance is on average 10% larger than the theoretically predicted

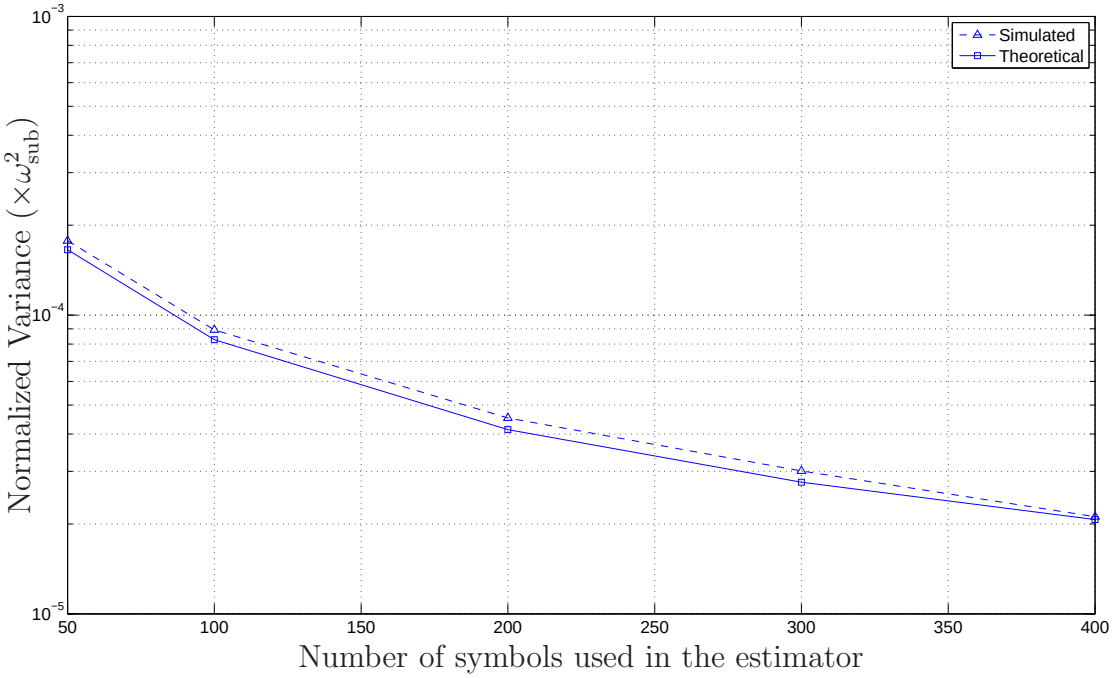

Figure 4.7: Effect of varying the number of symbols used in the CFO estimator

variance. This difference is attributed to the assumptions made in the analysis of Chapter 3. Given the number of assumptions in the variance calculations, this factor of approximately 0.5 dB is very reasonable. Therefore, Figure 4.6 confirms that the length of the cyclic prefix does indeed effect the estimator variance as predicted.

4.3.2 Effects of the Number of Symbols Used in the Estimator

Changing the number of symbols used in the CFO estimator provides the primary means of adjusting its variance to meet performance specifications. While holding all other parameters constant, the number of symbols used to estimate the CFO was varied. Figure 4.7 compares the theoretically predicted and simulated variances as a function of the number of symbols.

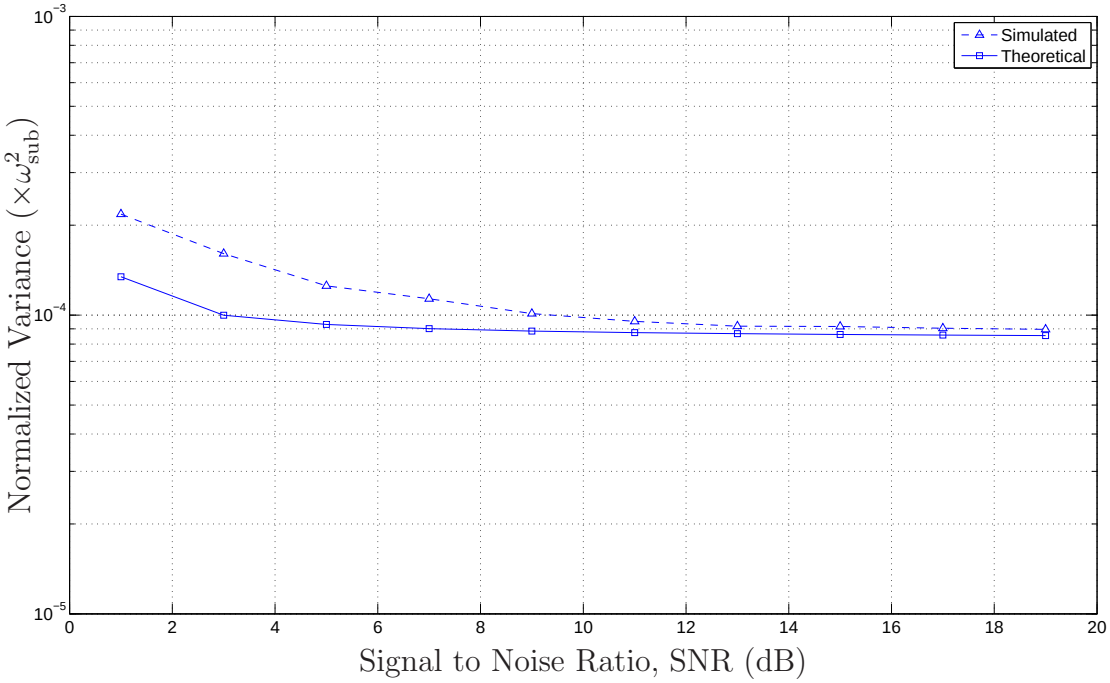

Figure 4.8: Effect of varying the SNR

Figure 4.7 illustrates that the variance changes as $1/N_{\text{sym}}$, where N_{sym} is the number of symbols processed. Again, the simulated variance is roughly 10% larger than the theoretical variance due to the assumptions made in Chapter 3.

4.3.3 Effects of Additive White Gaussian Channel Noise

In the analysis of Section 3.3.2, two components to the noise of the estimate are considered. Specifically, these components are pattern-dependent self-noise and AWG channel noise. In order to verify the effects of the AWGN component, the channel SNR was varied while holding all other parameters constant.

Figure 4.8 compares the simulated and theoretical variances as a function of SNR. At high SNRs, there is again a difference of approximately 10% between the simulated and the theoretical variances for the majority of the simulations. At very low signal

to noise ratios, this difference increases until the simulated variance is approximately 70% larger than the theoretical variance at an SNR of 1.

This significant difference at low SNRs is attributed to the model used for the noise on the estimated power spectrum. Specifically, the noise at the output of the power spectrum estimator is modeled as the self noise of the power spectrum estimator without considering channel noise plus the averaged AWG channel noise. When the channel noise is moderate, which is the case at common operating SNRs of 10 dB and above, this is a reasonable approximation. However, for very low SNRs with much higher channel noise, the AWGN will significantly effect the self noise of the power spectrum estimator. These effects were ignored in order to greatly simplify the mathematics.

For SNRs above 10dB, the theoretical variance predicts the observed simulated results very well. As the SNR increases, less improvement in variance performance is observed in Figure 4.8. This is consistent with the mathematical variance expression as the contribution from the AWG component of the noise becomes overshadowed by the estimator self-noise.

4.3.4 Effects of the Modulation Type

The pattern-dependent component of the noise is based upon modulation of received signals. When averaging a large number of OFDM symbols, the mean of this noise is zero. Given the assumptions made in the analysis of Chapter 3, the pattern-dependent noise of the CFO estimator should not change for higher order QAM modulation schemes. Simulations testing various sub-carrier modulation schemes, specifically BPSK, QPSK, 16-QAM, and 64-QAM, confirm this prediction. The CFO estimator variance in all test cases was the same. This is a distinguishing characteristic as the performance of some existing CFO recovery algorithms diminishes with

higher order modulation schemes.

4.3.5 Effects of the Carrier Frequency Offset Value

The variance of the power spectrum estimate presented in Figure 4.4 displays distinct periodicity that changes with the power spectrum estimator's mean value at any given frequency. This introduces a slight bias into the final theoretical CFO estimator variance. When there is no CFO, the bias is zero. When the CFO is at its maximum value of $\pm 1/2$ of the sub-carrier spacing, the theory predicts that the bias is a factor of more than 200 smaller than the sum of the other terms. A set of simulations was performed by varying the carrier frequency offset in increments of $0.05\omega_{\text{sub}}$ from -0.5 to $0.5\omega_{\text{sub}}$, where ω_{sub} is the sub-carrier spacing. These simulations confirm that the bias is negligible and not notably effect the variance of the proposed estimator.

5. RESULTS

Up to this point, the theoretical analysis and verification have been presented with the assumption of a flat AWGN channel. However, given that one of the major attractions of OFDM systems are their robustness in the face of multipath, practical channels will experience frequency selective rather than flat fading. In this chapter, the MSE of the proposed carrier frequency offset estimator will be examined when applied to a series of standard test channels.

In order to provide a context for evaluating the performance of the carrier frequency offset estimation algorithm proposed in this work, a comparison to other algorithms in the literature is carried out. Two alternative approaches to the problem of blind CFO estimation will be briefly examined. Sample results for each method are presented and are compared to similar results from the estimator proposed in Chapter 3. As previously mentioned, the performance characteristic of interest is the MSE of each method's CFO estimator.

Finally, limits for the parameters used in the algorithm are established to meet the requirements of the IEEE 802.16 standard.

5.1 Simulation Setup

The following simulations use a similar set of parameters as those used in Section 4.1. As before, the test system is based upon the IEEE 802.16a standard specifications with the specific system parameters listed in Table 4.1. Unlike the previous setup, however, the following results include frequency selective multipath channels.

5.1.1 Channel Characteristics

The characteristics of wireless channel models are heavily dependant upon the architecture of a specific system. In [24], the IEEE 802.16a Task Group presented a set of typical channel models for fixed wireless applications in three common terrain types. The models themselves are Standford University Interim (SUI) channel models with parameters selected based upon the system specifications of the IEEE 802.16 standard.

For the purposes of this work, one channel model for each key terrain type has been selected from [24]. Specifically, SUI models 1 (hilly with heavy tree density), 4 (intermediate path-loss condition), and 5 (flat terrain with light tree density) are chosen. These models also correspond to low, moderate, and high delay scenarios, respectively. In each case, the omnidirectional antenna cases are chosen.

The results presented in this chapter analyze the algorithm performance when processing a relatively low number of symbols. It is assumed that the channel is time invariant during each individual simulation trial. This means Doppler and statistical time-varying fading effects are not included in the simulated channel models.

The general-case frequency selective channel models are implemented as tapped delay lines. Each tap represents one or more paths that have a specific delay. The delay of each tap is fixed as doppler effects have been omitted. The number of taps, their attenuation, and their delays are taken from page 16 in [24]. Each delay path has a different random phase. These phases are randomly chosen for each trial then held constant for the duration of the trial. The relevant parameters for each of these three models are presented in Table 5.1.

Figures 5.1, 5.2, and 5.2 show several examples of the magnitude squared of the channel frequency response, $|H(e^{j\omega})|^2$ for the three channel types used in the sim-

Table 5.1: Multipath Channel Model Parameters

SUI-1 Channel	**Tap 1**	**Tap 2**	**Tap 3**	**Units**
Delay	0	0.4	0.9	μs
Power	0	-15	-20	dB

SUI-4 Channel	**Tap 1**	**Tap 2**	**Tap 3**	**Units**
Delay	0	1.5	4	μs
Power	0	-4	-8	dB

SUI-5 Channel	**Tap 1**	**Tap 2**	**Tap 3**	**Units**
Delay	0	4	10	μs
Power	0	-5	-10	dB

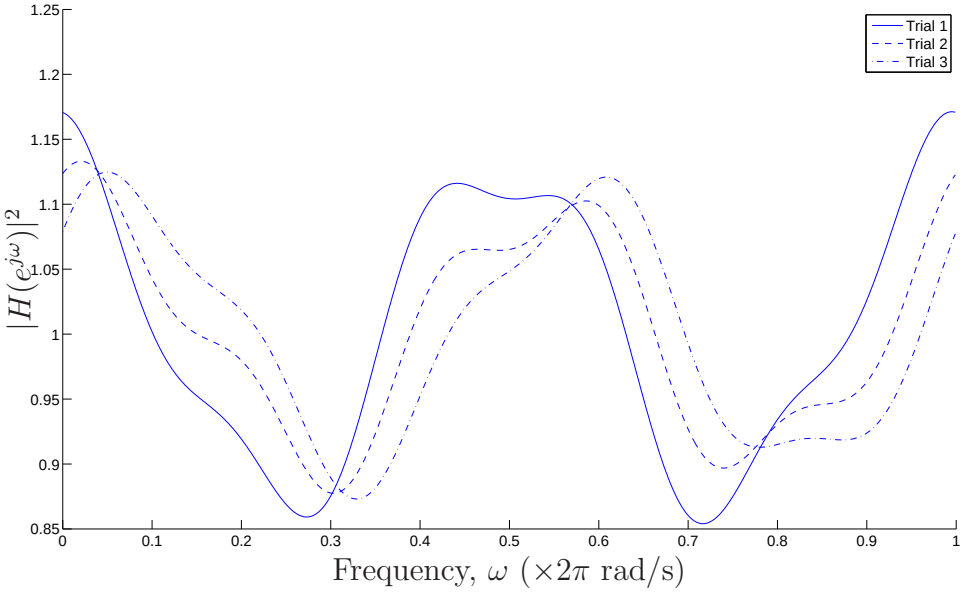

Figure 5.1: Sample Frequency response for SUI-1 low delay channel model (hilly terrain with high tree density)

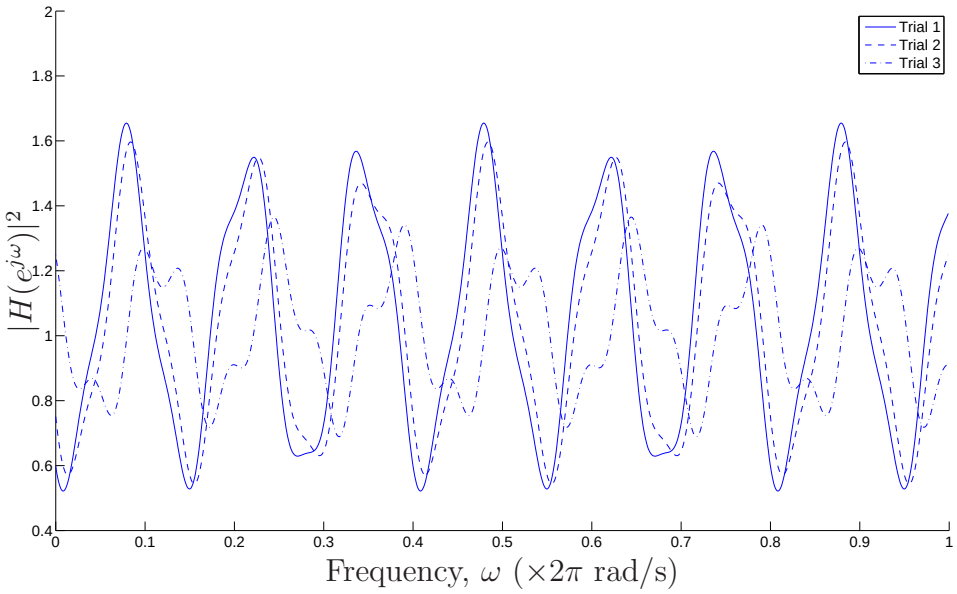

Figure 5.2: Sample Frequency response for SUI-4 moderate delay channel model (intermediate path-loss condition)

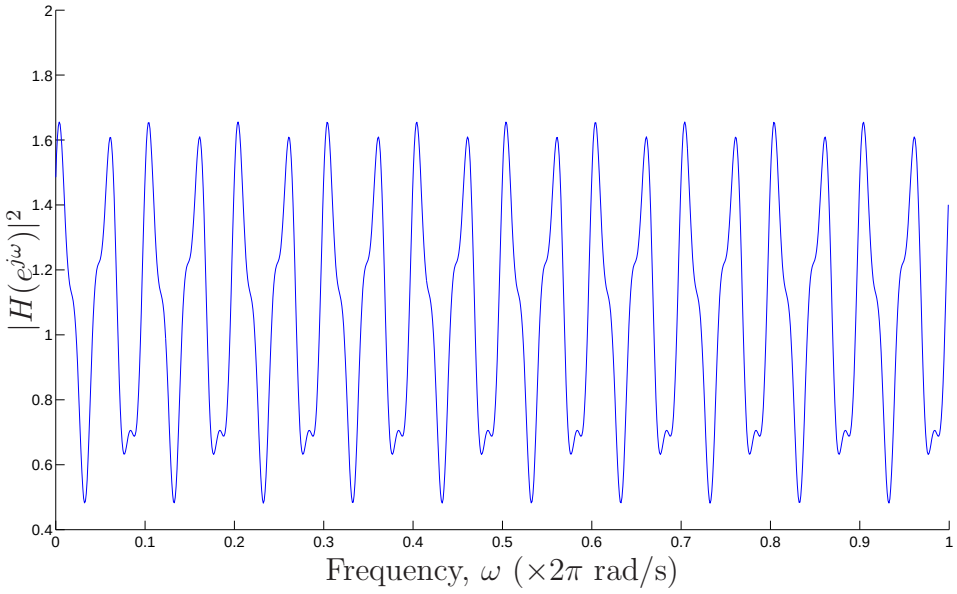

Figure 5.3: Sample Frequency response for SUI-5 high delay channel model (flat terrain with light tree density)

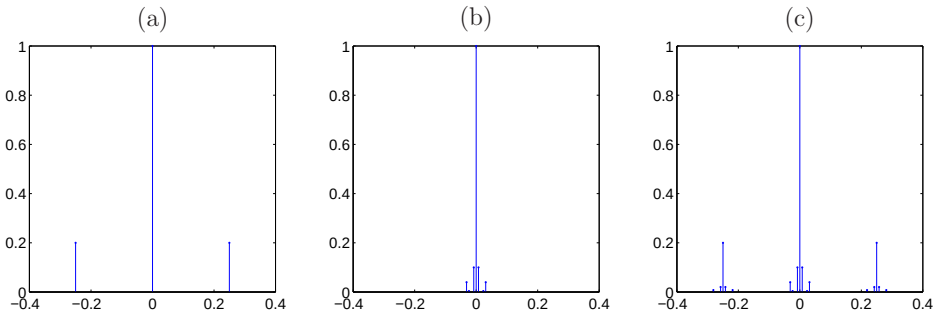

Figure 5.4: (a) Fourier series of the raised sinusoidal power spectrum; (b) Fourier series of a multipath channel's frequency response; (c) Fourier series of the received power spectrum for a multipath channel

ulations. Only one trace is shown in Figure 5.3 as to do otherwise would make it too busy. In each of these three channels, the exact shape of the channel's frequency response changes based upon the phase of each delay path. While a different set of phases are randomly chosen for each trial, the frequency responses for all trials are all roughly periodic. This facilitates modeling them as a Fourier series to predict their effects upon the proposed CFO estimator.

As previously described, the proposed algorithm calculates the Fourier series coefficients of the received signal's power spectrum, which takes the form of a raised cosine. These coefficients are shown in Figure 5.4(a). When considering a multipath channel, the power spectrum of a flat channel is multiplied by $|H(e^{j\omega})|^2$. The Fourier series for the resulting power spectrum with multipath interference will be a convolution of the flat power spectrum's Fourier series with the Fourier series of the multipath frequency response $|H(e^{j\omega})|^2$. Figure 5.4(b) shows the Fourier series of the multipath frequency response, and Figure 5.4(c) shows the result of this convolution.

In all three standard multipath channel models, the Fourier series of $|H(e^{j\omega})|^2$ has no significant frequency content near the frequency of the power spectrum's raised

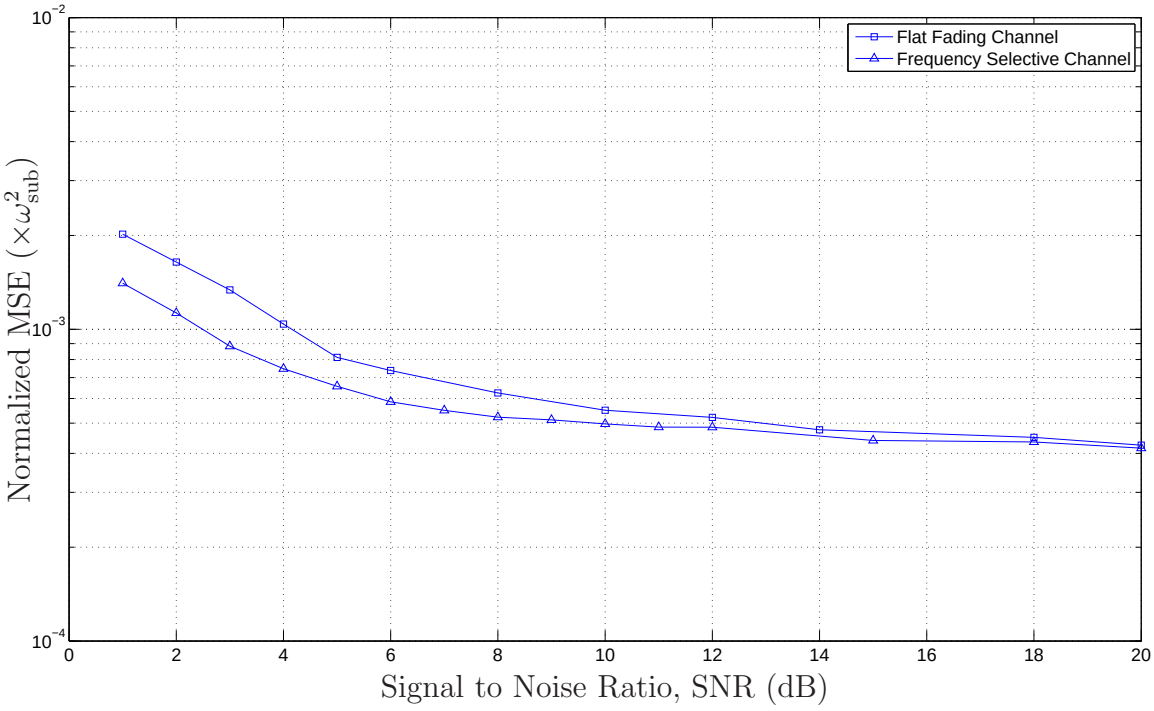

Figure 5.5: Effects of multipath on simulated CFO estimator performance

sinusoidal component. For example, even in the worst case SUI-5 channel, the Fourier coefficients of $|H(e^{j\omega})|^2$ near the frequency of the power spectrum's raised sinusoid are approximately 4 orders of magnitude smaller than the coefficients of the sinusoid itself. As such, the impact of a multipath channel on the mean squared error of the carrier frequency offset estimator is small. This impact is illustrated in Figure 5.5.

Figure 5.5 compares the MSE of the CFO estimator for two channels. One is a flat channel and the other is the SUI-5 channel which is frequency selective. The SUI-5 channel contains the highest frequency content of the three channels, making it the most likely to interfere with the estimator and therefore a worst case channel. The multipath causes a small performance degradation for low SNR. This suggests that the algorithm does not require that a channel equalizer to proceed it to function

properly. As such, the performance equation derived for a flat channel performs reasonably well for a frequency selective channel.

5.2 Algorithm Performance Comparisons

5.2.1 CFO Estimation Based on Cyclic Prefix Correlation

The first approach to blind carrier frequency offset recovery, presented in van de Beek [15] and further explored in Ahmadi [12] takes advantage of the cyclic prefix contains repeated samples from the end of the symbol as described in Section 2.3.2.

When considering a flat fading AWGN channel, the received signal $r(k)$ can be expressed as:

$$r(k) = s(k-\theta)e^{j2\pi\Delta\omega k/N} + n(k) \tag{5.1}$$

where $s(k)$ is the transmitted signal, θ is the carrier phase offset, $\Delta\omega/N$ is the normalized carrier frequency offset, and $n(k)$ is AWGN noise.

If $2N+L$ consecutive received samples are observed, one complete OFDM symbol with cyclic prefix (combine length $N+L$) will be contained within the observation. The correlation between these samples can be expressed as:

$$E[r(k)r^*(k+m)] = \begin{cases} \sigma_s^2 + \sigma_n^2 & m = 0 \\ \sigma_s^2 e^{-j2\pi\Delta\omega} + \sigma_n^2 & m = N \\ 0 & \text{otherwise} \end{cases} \tag{5.2}$$

where σ_s is the variance of the transmitted signal, $s(k)$, and σ_n is the variance of the noise, $n(k)$. Equation (5.2) illustrates that the correlation between each sample of the cyclic prefix and its corresponding sample at the end of the OFDM symbol is dependant upon the CFO. Using this property, [15] develops a log-likelihood function for maximum likelihood (ML) estimation of the phase and frequency offsets. This method of estimation was designed with the assumption of either a flat fading channel

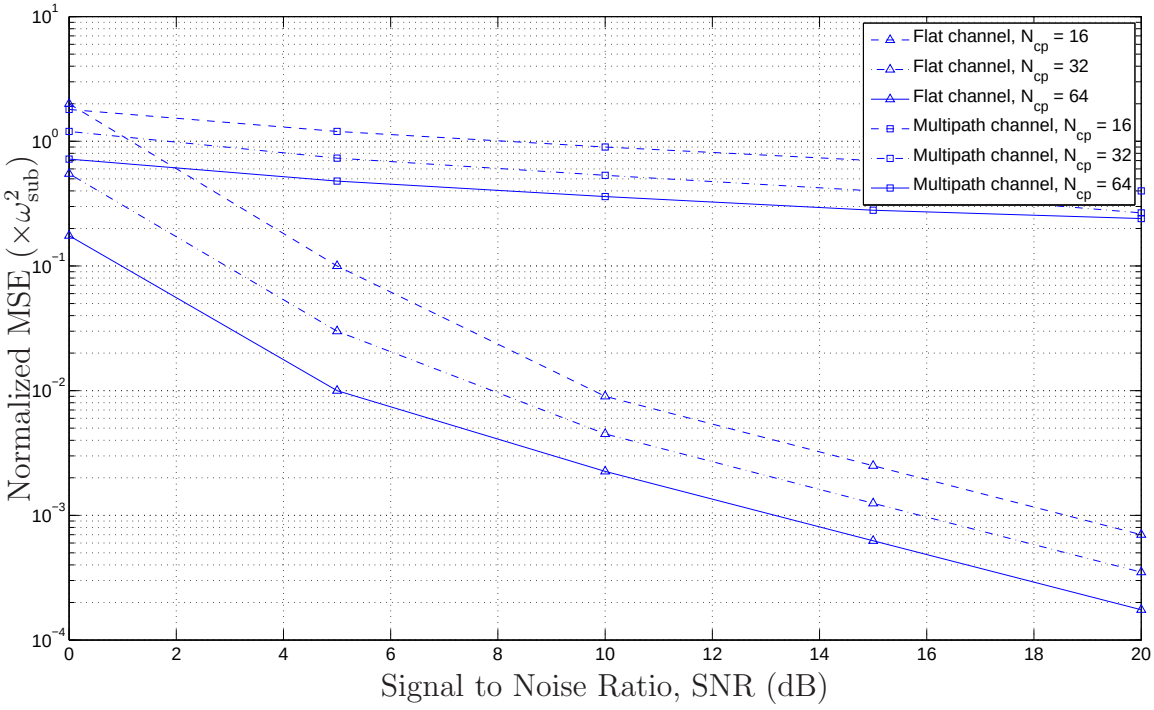

Figure 5.6: Performance of cyclic prefix correlation based CFO estimator

or prior high-quality channel equalization. Although the algorithm can still be applied to a multipath channel, its performance will be heavily degraded. This is due to the significantly more complex correlation structure of a given channel that cannot be generally accounted for mathematically.

The cyclic prefix based algorithm algorithm is simulated for the standard IEEE 802.16 test system outlined above both with and without multipath. Figure 5.6 shows the MSE of van de Beek's [15] CFO estimator for a set of sample results.

Practically, the cyclic prefix length is fixed by the IEEE 802.16 standard to one of three possible values based upon channel conditions. As such, the algorithm is limited to varying the number of symbols averaged for tuning purposes. However, the complex correlation structure of a multipath channel creates an error floor for

the algorithm that is quickly reached. In order to compensate for this, [15] suggests a hybrid between traditional data-aided and blind algorithms. [12] explores such a hybrid using superimposed pilots. Conventionally, an algorithm is either data-aided or blind. Such classification would have this so called hybrid algorithm in the class of data-aided. As such, this avenue will not be further discussed.

5.2.2 CFO Estimation Based on Subspace Structure

The wireless IEEE 802.16 standard includes a number of null sub-carriers as a guard band in order to limit out of band emissions and to prevent adjacent channel interference. These null carriers, combined with the inherent orthogonality between sub-carriers in an OFDM symbol, creates a shift-invariant algebraic structure in the received signal. A number of MUSIC-like [18] and ESPRIT-like [19] estimators are presented throughout the literature which exploit this structure to blindly estimate the CFO.

As the variations of these estimators have similar CFO MSE performance with equivalent Cramer-Rao lower bounds [1], only the results from the best performing implementation in [19] are presented. Specifically, Figure 5.7 shows the MSE of this estimator for the standard 802.16 test system described above.

As control parameters, the subspace methods adjust the number of virtual (null) sub-carriers or the number of symbols processed, N_{sym}. In the IEEE 802.16 standard, however, the number of nulls is fixed, which means that it can not be used as a control parameter. As such, Figure 5.7 only shows one set of operating curves for different values of N_{sym}.

Figure 5.7 illustrates that the subspace estimation method performs better than

[1]The Cramer-Rao lower bound gives the minimum achievable variance for an unbiased estimator

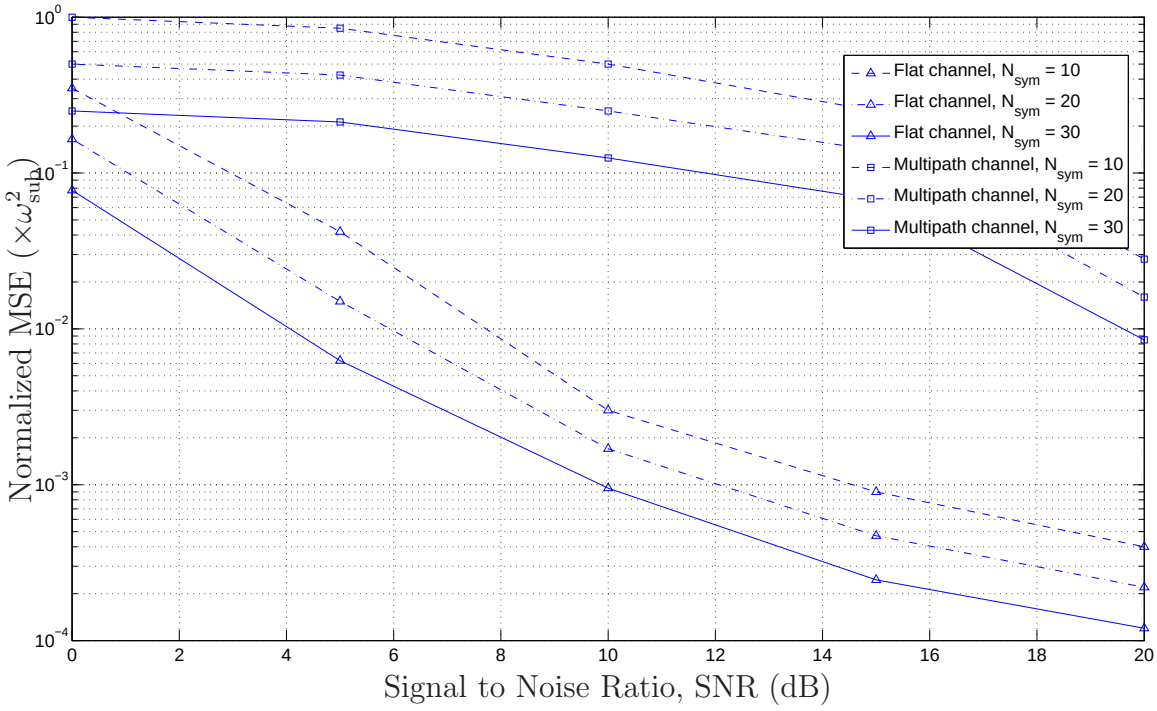

Figure 5.7: Performance of subspace structure based CFO estimator

the previous one in both flat and frequency selective channels, even with a relatively low number of symbols processed. For high SNR situations, the multipath performance of the subspace method does not experience the same type of error floor that was observed in the approach from Section 5.2.1 and only has moderate MSE performance degradation. That said, in lower to moderate SNR scenarios, a multipath channel again creates significant degradation in the MSE performance of Tureli's CFO estimator [19].

5.2.3 CFO Estimation based on Power Spectral Estimation

The carrier frequency offset estimation algorithm proposed in this work has a wide tuning range.

The performance of the proposed algorithm is compared to two algorithms that have been referenced. The number of symbols used in the estimator is selected to place the MSE performance in a range similar to the performances of the presented estimators in [15], [19], and [12].

Figure 5.8 shows the results for the SUI-4 channel model. The SUI-4 model represents a channel with intermediate path-loss and a moderate delay. A cyclic prefix length of 32 samples is used as specified in the IEEE 802.16 standard. Even when the estimate is obtained using a relatively low number of symbols, the performance exceeds that of the van de Beek algorithm [15] which is cyclic prefix correlation based. In low to moderate SNR operating conditions, the approach presented in this work also outperforms Tureli's super resolution subspace based algorithm [19]. However, in very high SNR scenarios, Tureli's algorithm performs better. This result is expected as super-resolution MUSIC and ESPRIT-like algorithms tend to have excellent performance at SNRs above some threshold. Many practical systems operate in the low to moderate SNR ranges, making the proposed algorithm a better choice.

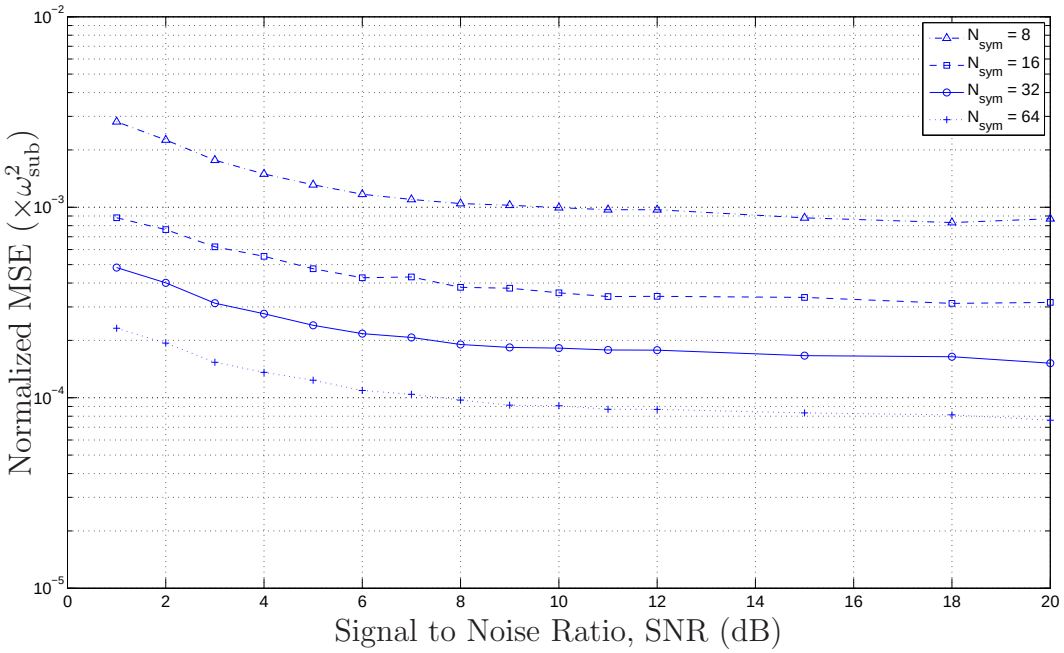

Figure 5.8: Proposed CFO estimator performance (SUI-4 channel)

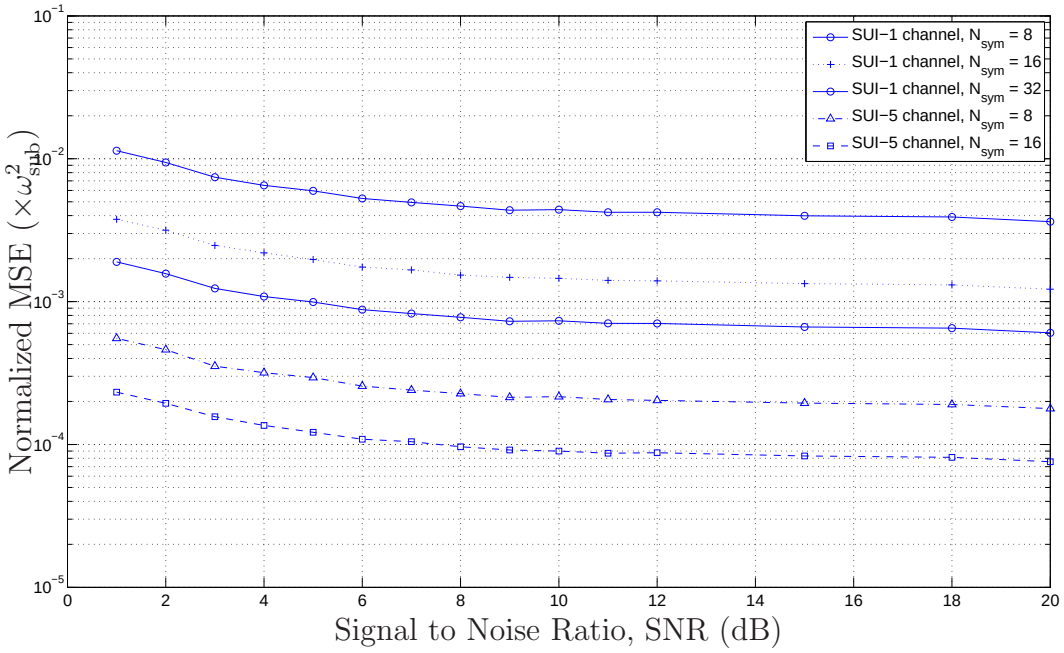

Figure 5.9: Proposed CFO estimator performance (SUI-1 and SUI-5 channels)

Figure 5.9 shows the MSE results for SUI-1 and SUI-5 channels. The SUI-1 channel models a low delay. The IEEE 802.16 standard requires only a 16 sample cyclic prefix for such channels. The SUI-5 channel models a high delay. The IEEE 802.16 standard requires a 64 sample cyclic prefix for such channels. The performance of the proposed algorithm performance significantly exceeds that of other algorithms in the SUI-5 channel due to the large cyclic prefix. Even in the worst case low delay channel, the performance still rivals the subspace solution at low to moderate SNR levels. Note that in both Figure 5.8 and 5.9 the performance does not scale exactly as $1/N_{\text{sym}}$. As the number of symbols processed increases, however, the approximation based on assumptions made in Chapter 3 become more accurate, and the algorithm does scale as expected for tuning purposes.

5.3 Performance Requirements for Practical Applications

The previous section illustrates a set of results comparing the performance of the proposed algorithm to other blind CFO recovery methods found within the literature. Given the low number of tuning options for the estimator presented in Section 5.2.1, its performance characteristics determine the MSE range selected for comparison purposes above. Unfortunately, the performance in this range is not sufficient for practical IEEE 802.16 based systems.

The IEEE 802.16 standard specifies a maximum carrier frequency offset tolerance of 2% of the subcarrier spacing (defined in Chapter 3 as ω_{sub}) for an OFDM physical layer. In order to calculate the system parameters necessary to meet this requirement, the variance of the estimator will be used. Unlike the stated maximum threshold, variance is a much more mathematically tractable quantity. Although it is difficult to say with 100% certainty that this requirement will be met in every case, choosing a sufficiently low variance will ensure that it is met in the a very high percentage of the

Table 5.2: Tuning Parameters for Practical Performance Levels

CP Length (samples)	**Calculated N_{sym} Required** (symbols)	**Resulting CFO Estimator MSE** ($\times\omega_{\text{sub}}^2$)
16	1850	$15.5\text{x}10^{-6}$
32	480	$15.8\text{x}10^{-6}$
64	140	$15.2\text{x}10^{-6}$

time. We will use 5 standard deviations as a benchmark for always meeting the error requirement such that $5\sigma \leq 0.02\omega_{\text{sub}}$. While some practical applications may not require quite that level of accuracy, 5 standard deviations ensures that 99.99994267% of all results will satisfy the IEEE 802.16 requirements. This means that the MSE of the CFO estimate should be $\sigma^2_{\text{CFO}_{\text{norm}}} \leq 16\text{x}10^{-6}$.

Selecting an operating point at an SNR of 10 dB, the number of symbols that must be processed to satisfy this criteria for each of the three possible cyclic prefix values is calculated with Equation 3.76 from page 50. The 10% difference between the simulated and theoretical variances that was observed in Chapter 4 is taken into account in the variance calculation. A 10% degradation in MSE performance due to the effects of multipath is also considered.

Figure 5.10 shows the MSE of the CFO estimator with the calculated parameters listed in Table 5.2. Even with the very strict performance requirement of 5 standard deviations, the number symbols required by the estimator is quite reasonable given current transmission speeds and memory capacities. The observed performance is particularly good in high delay channels that require longer cyclic prefixes.

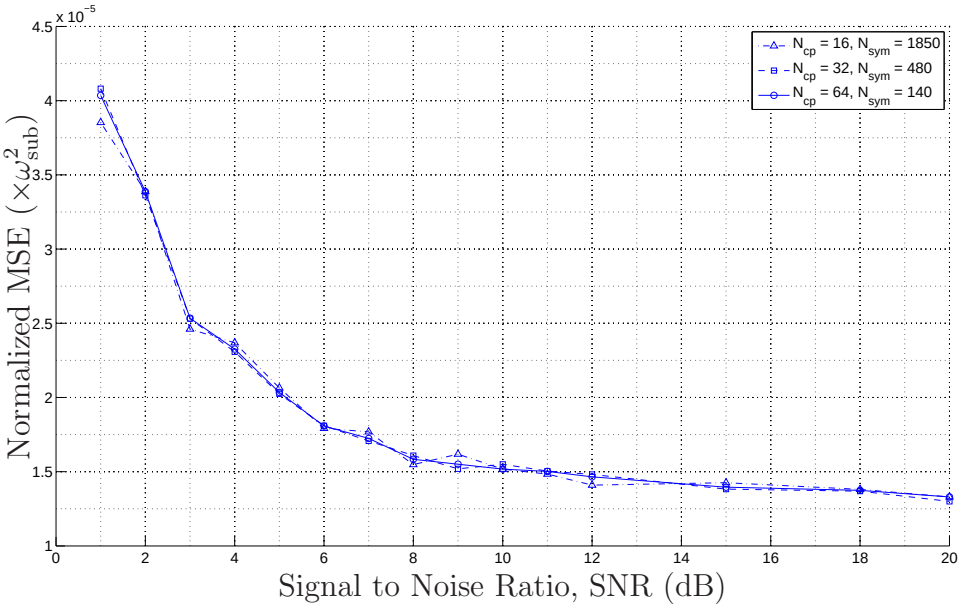

Figure 5.10: Proposed algorithm performance for practical pequirements

6. CONCLUSIONS AND FUTURE WORK

6.1 Conclusions

The objective of this thesis was to develop and to analyze an algorithm for blind CFO recovery suitable for use with a practical zero-IF OFDM telecommunications system. OFDM is more sensitive to carrier frequency offsets than other modulation techniques like QAM. CFOs significantly degrades the SNR at the output of the receiver.

The proposed algorithm exploits the baseband power spectrum of the received OFDM signal. This power spectrum, which has units V^2, is shown to be a raised sinusoid with three key characteristics.

1. The amplitude of the power spectrum's sinusoidal component depends upon the length of the cyclic prefix.
2. The period of the sinusoidal component, which in this case has units radians/sample, is equal to the sub-carrier spacing.
3. The phase of the sinusoidal component depends on the carrier frequency offset in the receiver's local oscillator.

The proposed algorithm exploits these characteristics in three stages. In the first stage, the power spectrum of the received signal is estimated. It is shown that the optimum spectral resolution for this estimate has 4 samples per sub-carrier spacing.

The second stage deals with the sub-carrier devoid guard band. Not all of the

spectrum in the IEEE 802.16 standard is allocated to data carrying sub-carriers. The presence of the null carriers at DC and in the guard band necessitates the removal of samples from the data carrying sub-carriers that border these nulls. At each data to null transition, four data samples must be removed. After the samples associated have been removed, the remaining spectrum is concatenated to form a raised sinusoid with continuous phase.

The third stage of the proposed algorithm estimates the phase shift of the sinusoidal component of this concatenated signal. This is done using Fourier series coefficients. The carrier frequency offset on the received baseband signal was earlier shown to be proportional to the carrier frequency offset.

The concatenated power spectrum is theoretically analyzed to get the mean and variance of the proposed carrier frequency offset estimator. Simulation verifies the theoretical expressions for the mean and the variance of the proposed CFO estimator. The verification was quite thorough. The important algorithm parameters, which include the cyclic prefix length, the number of symbols used in the estimator, the channel SNR, the modulation type, and the carrier frequency offset, were varied. As the parameters are changed, variance changes in close agreement with the theoretical variance. Specifically, the simulated variance was approximately 0.5 dB larger than the theoretically expected value.

Simulation confirms the theoretical expression which indicates that the modulation type and the carrier frequency offset do not effect the variance. Invariance to modulation type is a salient attribute of the proposed algorithm as the variance of some existing algorithms increases with higher order modulation schemes.

The practical performance of the algorithm is characterized by performing simulations in a set standardized multipath test channels. The standardized channels used

are based upon the Stanford University Interim channel models as specified in the IEEE 802.16 standard. The channel models are characterized, and the worst case scenario is compared to the performance of the algorithm in a flat channel. The impact of this channel on the the variance of the estimator is shown to be small, particularly around a common operating SNR of 10 dB.

For purposes of comparison, two other blind CFO recovery algorithms from the literature were evaluated. The two algorithms considered were van de Beek's cyclic prefix correlation based estimator [15] and Tureli's ESPRIT-like super-resolution subspace based algorithm [19]. In a flat or equalized channel at an operating SNR of 10 dB, the performance of the proposed estimator is shown to be roughly equivalent to those of the cyclic prefix correlation and ESPRIT-like based algorithms. However, both of these alternative algorithms display significant performance degradation in multipath channels. For the worst case channel model used in this work, the proposed algorithm has a variance roughly 100 times lower than the van de Beek and Tureli algorithms at an SNR of 10 dB.

One measure for the performance of the system was suggested as the number of symbols used to obtain a sufficiently accurate estimate. In the IEEE standard, the maximum tolerable carrier frequency offset is specified as 2% of the sub-carrier spacing. In order to limit the estimator error to less than 2% of the sub-carrier spacing with a very high probability, the variance of the estimator was restricted by $5\sigma \leq 0.02\omega_{\text{sub}}$ where ω_{sub} is the sub-carrier spacing. Using the mathematically derived variance expression with the empirically derived scaling factor of 24, the number of symbols that must be used to ensure that the variance is below threshold is 140, 480, 1850 for cyclic prefix lengths of 64, 32, and 16 samples, respectively. It is observed that the algorithm performs particularly well for long cyclic prefixes, even though these prefixes are typically associated with high delay channels.

6.2 Future Work

Compared to other blind CFO recovery algorithms in the literature, the proposed estimator is shown to perform very well in frequency selective channels. That said, improvements to the proposed algorithm's performance and mathematical characterization could be investigated as a source of future work. In order to enhance performance, alternate methods of spectral estimation could be examined. One example would be to use overlapping and possibly windowed data segments as is done in Welch's method of spectral estimation [32]. It would also be beneficial to analyze the variance of the estimator in greater detail given that overlapping and windowed segments would introduce significantly more complex correlation between segments. Similarly, the effects of multipath channels could be included throughout the entire mathematical analysis.

References

[1] J. Sevenhans et. al., "Trends in silicon radio large scale integration: Zero IF receiver! Zero I & Q transmitter! Zero discrete passives!", *IEEE Communications Magazine*, vol. 38, pp. 142–147, Jan 2000.

[2] Leon W. Couch II, *Digital and Analog Communication Systems*, Prentice Hall, Inc., 6th Edition, 2001.

[3] D.G. Tucker, "The History of the Homodyne and the Synchrodyne", *Journal of the British Institution of Radio Engineers*, pp. 143–154, April 1954.

[4] B. Razavi, "Design considerations for direct conversion receivers", *IEEE Transactions on Circuits and Systems II: Analog and Digital Signal Processing*, vol. 44, pp. 428–435, Jun 1997.

[5] S. Samadian et. al., "Demodulators for a zero-IF Bluetooth receiver", *IEEE Journal of Solid-State Circuits*, vol. 38, pp. 1393–1396, Aug 2003.

[6] Na Zhao et. al., "Zero-IF for GSM transmitter applications", volume 3, pp. 1512–1514. IEEE, Apr 2008.

[7] K.J. Richter, "Zero IF satellite tuners for DBS", *IEEE Transactions on Consumer Electronics*, vol. 44, pp. 1367–1370, Nov 1998.

[8] B. Saltzberg, "Performance of an Efficient Parallel Data Transmission System", *IEEE Transactions on Communications*, vol. 15, pp. 805–811, Dec 1967.

[9] S. Fouladifard and H. Shafiee, "Frequency offset estimation in OFDM systems in presence of IQ imbalance", volume 3, pp. 2071–2075. IEEE, May 2003.

[10] Mingqi Li and Wenjun Zhang, "A novel method of carrier frequency offset estimation for OFDM systems", *IEEE Transactions on Consumer Electronics*, vol. 49, pp. 965–972, Nov 2003.

[11] Zhongshan Zhang; Keping Long; Yuanan Liu, "Complex efficient carrier frequency offset estimation algorithm in OFDM systems", *IEEE Transactions on Broadcasting*, vol. 50, pp. 159–164, Jun 2004.

[12] Malihe Ahmadi, "Channel estimation, data detection and carrier frequency offset estimation in OFDM systems", Master's thesis, Dec 2007.

[13] P. Moose, "A technique for orthogonal frequency division multiplexing frequency offset correction", *IEEE Transactions on Communications*, vol. 44, pp. 2908–2914, Oct 1994.

[14] Erchin Serpedin et. al., "Blind channel and carrier frequency offset estimation usingperiodic modulation precoders", *IEEE Transactions on Signal Processing*, vol. 48, pp. 2389–2405, Aug 2000.

[15] Jan-Japp van de Beek et al., "ML estimation of time and frequency offset in OFDM systems", *IEEE Transactions on Signal Processing*, vol. 45, pp. 1800–1805, Jun 1997.

[16] Biao Chen and Hao Wang, "Blind estimation of ODFM carrier frequency offset via oversampling", *IEEE Transactions on Signal Processing*, vol. 52, pp. 2047–2057, Jul 2004.

[17] T.M. Schmidl and D.C. Cox, "Blind synchronization for OFDM", *Electronics Letters*, vol. 33, pp. 113–114, Jan 1997.

[18] H. Liu and U. Tureli, "A high-efficiency carrier estimator for OFDM communications", *IEEE Communications Letters*, vol. 2, pp. 104–106, Apr 1998.

[19] Ufuk Tureli; Hui Liu; Michael D. Zoltowski, "OFDM blind carrier offset estimation: ESPRIT", *IEEE Transactions on Signal Processing*, vol. 52, pp. 1459–1461, Sep 2000.

[20] IEEE Computer Society, IEEE Microwave Theory and Techniques Society, *IEEE Standard for Local and metropolitan area networks-Part 16: Air Interface for Fixed Broadband Wireless Access Systems*, IEEE, Oct 2004.

[21] Brian Minnis and Paul Moore, "A re-configurable receiver architecture for 3G mobiles", pp. 187–190. IEEE, 2002.

[22] P.M. Stroet et. al., "A zero-IF single-chip transceiver for up to 22Mb/s QPSK 802.11b Wireless LAN", volume 37, pp. 204–205. IEEE, 2001.

[23] Eric Pellet, "Signal Distortion Cause By Tree foliage in a 2.5 GHz Channel", Master's thesis, Nov 2003.

[24] V. Erceg et. al., *Channel Models for Fixed Wireless Applications*, IEEE, 2003.

[25] Yen-Ju Huang and Shyue-Win Wei, "Modified guard band power detection methods for OFDM frequency offset recovery", volume 4, pp. 2277–2281. IEEE, Oct 2003.

[26] Herbert B. Dwight, *Table of Integrals and Other Mathematical Data*, The McMillan Company, 4th Edition, 1961.

[27] S.L. Marple Jr., "A tutorial overview of modern spectral estimation", pp. 2152–2157. IEEE, May 1989.

[28] L. Isserlis, "On a formula for the product-moment coefficient of any order of a normal frequency distribution in any number of variables", *Biometrika*, vol. 12, pp. 134–139, 1918.

[29] Kamalesh Kumar Sharma and Shiv Dutt Joshi, "Time delay estimation using fractional Fourier transform", *Signal Processing*, vol. 87, pp. 853–865, 2007.

[30] C. Knapp and G. Carter, "The generalized correlation method for estimation of time delay", *IEEE Transactions on Acoustics, Speech and Signal Processing*, vol. 24, pp. 320–327, 1976.

[31] J. Eric Salt and Arthur G. Wacker, "Optimistic and pessimistic approximations to variance of time delay estimators", *IEEE Transactions on Acoustics, Speech and Signal Processing*, vol. 37, pp. 634–341, May 1989.

[32] P.D. Welch, "The use of fast fourier transform for the estimation of power spectra: A method based on time averaging over short, modified periodograms", *IEEE Trans. Audio Electroacoust*, vol. AU-15, pp. 70–73, June 1967.

A. MATLAB SOURCE CODE

The following MATLAB source code was used in Chapters 4 and 5 as a reference for setting up simulations of the proposed algorithm. Parameters listed are the defaults listed in Table 4.1.

```
%%%%%%%%%%%%%%%%%%%%%%%%%%%%%%%%%%%%%%%%%%%%%%%%%%%%%%%%%%%%%%%%%%%%%%%%%%%%
% Simulation Parameters
%%%%%%%%%%%%%%%%%%%%%%%%%%%%%%%%%%%%%%%%%%%%%%%%%%%%%%%%%%%%%%%%%%%%%%%%%%%%
N_TRIALS = 10000; % Number of trials to determine variance of the estimate
N = 256; % IFFT length used in the transmitter
N_USED = 200; % Number of sub-carrier frequencies used per symbol
              % Restricted to even numbers in this file
              % 200 is the number specified in IEEE 802.16
              % The placement of these used sub-carriers is also
              % specified in the standard
N_SYMBOLS = 100; % Number of Symbols used in the estimator
N_CP = 32; % Cyclic Prefix length
ALPHA = 4; % ALPHA * N is the input data segment length used in the
           % power spectrum estimator
CFO_percent = 0.2; % Carrier frequency offset specifies as a percentage of
                   % the sub-carrier spacing
k = 2;  % Modulation index, M = 2^k
        % 2 for QPSK, 4 for 16-QAM, etc...

% Calculated parameters
CFO = CFO_percent * 2*pi*1/N; % Carrier Frequency Offset
N_SAMPLES = N_SYMBOLS * (N+N_CP); % Total number of samples transmitted
bits_r = ceil(k/2); bits_i = floor(k/2); d = sqrt(6/(2^k-1));

% Initialize a data matrix to store results over multiple trials
```

```
Saved_Pxx = zeros(N_TRIALS,N*ALPHA);


%%%%%%%%%%%%%%%%%%%%%%%%%%%%%%%%%%%%%%%%%%%%%%%%%%%%%%%%%%%%%%%%%%%%%%%%%%%%
% Channel Parameters (SNR and random phase shift of the multiple paths
%%%%%%%%%%%%%%%%%%%%%%%%%%%%%%%%%%%%%%%%%%%%%%%%%%%%%%%%%%%%%%%%%%%%%%%%%%%%
SNR = 10; % Signal to Noise Ratio (dB)

% Multipath Phase Shifts
% Each tap in the multipath model has a different random phase
% in each trial
n_phase1 = rand(1, N_TRIALS);
n_phase2 = rand(1, N_TRIALS);
n_phase3= rand(1, N_TRIALS);


%%%%%%%%%%%%%%%%%%%%%%%%%%%%%%%%%%%%%%%%%%%%%%%%%%%%%%%%%%%%%%%%%%%%%%%%%%%%
% Simulation Body
%%%%%%%%%%%%%%%%%%%%%%%%%%%%%%%%%%%%%%%%%%%%%%%%%%%%%%%%%%%%%%%%%%%%%%%%%%%%
for trial_number = 1:N_TRIALS

% Display progress tracking for longer simulations
if(mod(trial_number,N_TRIALS/20) ==0)
    fprintf('Iteration Number: %s\n',num2str(trial_number));
end

%%%%%%%%%%%%%%%%%%%%%%%%%%%%%%%%%%%%%%%%%%%%%%%%%%%%%%%%%%%%%%%%%%%%%%%%%%%%
% Assemble Modulation Data (based on a transmit symbol energy of 1)
%%%%%%%%%%%%%%%%%%%%%%%%%%%%%%%%%%%%%%%%%%%%%%%%%%%%%%%%%%%%%%%%%%%%%%%%%%%%
% In order to reduce simulation times, the word value is
% directly generated instead of generating bits and
% then determining the value from there
complex_mod = d * ( ( randint(N_SYMBOLS, N_USED, 2^(k/2)) - (2^bits_r-1)/2 )
            + j*( randint(N_SYMBOLS, N_USED, 2^(k/2)) - (2^bits_i-1)/2 ) );
```

```
% Only 200 of the possible 256 sub-carriers are used.  Place the zeros in
% proper locations for the OFDM symbols.  Note that the horzcat function
% is used here for concatenation for clarity of display in the thesis.
complex_mod = horzcat(zeros(N_SYMBOLS,1),
                      complex_mod(:,1:N_USED/2),
                      zeros(N_SYMBOLS, N - N_USED - 1),
                      complex_mod(:, N_USED/2+1:N_USED));

%%%%%%%%%%%%%%%%%%%%%%%%%%%%%%%%%%%%%%%%%%%%%%%%%%%%%%%%%%%%%%%%%%%%%%%%%%%%
% Generate received time sequence
%%%%%%%%%%%%%%%%%%%%%%%%%%%%%%%%%%%%%%%%%%%%%%%%%%%%%%%%%%%%%%%%%%%%%%%%%%%%
x_n = ifft(complex_mod, N, 2);     % Take IFFT to create time sequence
x_n = [x_n(:, N-N_CP+1:N) x_n];    % Insert cyclic prefix
x_n = reshape(x_n.', 1, []);       % Reshape into a 1 dimensional vector
xr_n = exp(j*CFO*[1:N_SAMPLES]) .* x_n;     % Introduce CFO


%%%%%%%%%%%%%%%%%%%%%%%%%%%%%%%%%%%%%%%%%%%%%%%%%%%%%%%%%%%%%%%%%%%%%%%%%%%%
% Channel
%%%%%%%%%%%%%%%%%%%%%%%%%%%%%%%%%%%%%%%%%%%%%%%%%%%%%%%%%%%%%%%%%%%%%%%%%%%%
% Add AWGN (possibly fading channels at a later date)
if SNR ~= 0
    xr_n = awgn(xr_n,SNR,'measured');
end

% Un-comment the appropriate channel model.  "chan" is the variable
% directly used in the simulation.  "channel_model" is saved for other
% processing or display
chan = zeros(1,N_CP);
chan(1) = 1 * exp(j*2*pi*n_phase1(trial_number));   % 0 dB, random phase 1

% Low Delay
%   chan(2)= 0.1 * exp(j*2*pi*n_phase1(trial_number));
%   chan(5) = 0.0398 * exp(j*2*pi*n_phase1(trial_number));
%   channel_model(trial_number,:) = chan;
```

```
% Moderate Delay
chan(8)= 0.0316 * exp(j*2*pi*n_phase1(trial_number));
chan(20) = 0.01 * exp(j*2*pi*n_phase1(trial_number));
channel_model(trial_number,:) = chan;

% High Delay
%    chan(20)= 0.1 * exp(j*2*pi*n_phase1(trial_number));
%    chan(50) = 0.0398 * exp(j*2*pi*n_phase1(trial_number));
%    channel_model(trial_number,:) = chan;

chan = chan * CHANNEL_NORM; % Normalize the channel energy
xr_n = filter(chan, 1, xr_n); % Filter with the channel


%%%%%%%%%%%%%%%%%%%%%%%%%%%%%%%%%%%%%%%%%%%%%%%%%%%%%%%%%%%%%%%%%%%%%%%%%%%%%%%
% Power Spectrum Estimator
%%%%%%%%%%%%%%%%%%%%%%%%%%%%%%%%%%%%%%%%%%%%%%%%%%%%%%%%%%%%%%%%%%%%%%%%%%%%%%%
xlim = mod(length(xr_n), ALPHA*N); % May need to discard some samples
                                   % that do not fit exactly into an
                                   % even number of segments
xr_n = reshape(xr_n(1:length(xr_n)-xlim), ALPHA*N, []); % Segmentation
Pxx = abs(fft(xr_n,ALPHA*N)).^2;
Pxx = mean(Pxx,2);

Saved_Pxx(trial_number,:) = Pxx; % Save the power spectrum estimate in a
                                 % matrix for processing multiple trials

end % End the multi-trial loop.  The remainder of the simulation will
    % process all of the trials at once


%%%%%%%%%%%%%%%%%%%%%%%%%%%%%%%%%%%%%%%%%%%%%%%%%%%%%%%%%%%%%%%%%%%%%%%%%%%%%%%
% Information Band Isolator
%%%%%%%%%%%%%%%%%%%%%%%%%%%%%%%%%%%%%%%%%%%%%%%%%%%%%%%%%%%%%%%%%%%%%%%%%%%%%%%
```

```
info_range = [2*ALPHA+1:100*ALPHA 157*ALPHA+1:255*ALPHA];
N_ISO = size(info_range,2);
info = Saved_Pxx(:,info_range); info = squeeze(info);

%%%%%%%%%%%%%%%%%%%%%%%%%%%%%%%%%%%%%%%%%%%%%%%%%%%%%%%%%%%%%%%%%%%%%%%%%%%%%%%
% CFO Estimator
%%%%%%%%%%%%%%%%%%%%%%%%%%%%%%%%%%%%%%%%%%%%%%%%%%%%%%%%%%%%%%%%%%%%%%%%%%%%%%%
% Generate comparison signal to calculate the one specific Fourier
% series coefficient at the frequency of spectrum's sinusoidal component
n = [0:N_ISO-1];
x_compare = ones(N_TRIALS,1) * exp(j*2*pi*1/ALPHA*n);
x_out = info .* x_compare;

phase_shift = angle(mean(x_out.'));

% CFO normalized to one subcarrier spacing
est_cfo = (phase_shift)/(2*pi);
est_cfo_mean = mean(est_cfo)
est_cfo_var = var(est_cfo)

% calculate the theoretically predicted performance
M = N_SYMBOLS/ALPHA*(N+N_CP)/N;
gamma = N_ISO*sum((cos(2*pi*n/ALPHA+est_cfo_mean*2*pi/N).^2
            .*sin(2*pi*n/ALPHA+est_cfo_mean*2*pi/N).^2)/(M*N_ISO/2).^2);

theo_var  =
N_ISO/2*ALPHA^2/M/(N_ISO/2)^2/(2*(ALPHA-1)*N_CP/(N+N_CP))^2 + gamma
+ N_SIO/2/SNR/M/(N_ISO/2)^2/(2*(ALPHA-1)*N_CP/(N+N_CP))^2 ;

% normalized to one subcarrier spacing
theo_var = theo_var /(2*pi)^2
```